A&A 675, A119 (2023)
https://doi.org/10.1051/0004-6361/202245784
© The Authors 2023

Astronomy & Astrophysics

Large-scale velocity-coherent filaments in the SEDIGISM survey: Association with spiral arms and the fraction of dense gas

Y. Ge[1,2], K. Wang[2], A. Duarte-Cabral[3], A. R. Pettitt[4], C. L. Dobbs[5], Á. Sánchez-Monge[6], K. R. Neralwar[7], J. S. Urquhart[8], D. Colombo[7], E. Durán-Camacho[3], H. Beuther[9], L. Bronfman[10], A. J. Rigby[11], D. Eden[12], S. Neupane[7], P. Barnes[13,14], T. Henning[9], and A. Y. Yang[15,7]

[1] Department of Astronomy, School of Physics, Peking University, 5 Yiheyuan Road, Haidian District, Beijing 100871, PR China
[2] Kavli Institute for Astronomy and Astrophysics, Peking University, 5 Yiheyuan Road, Haidian District, Beijing 100871, PR China
e-mail: kwang.astro@pku.edu.cn
[3] School of Physics & Astronomy, Cardiff University, Queen's building, The parade, Cardiff, CF24 3AA, UK
[4] Department of Physics and Astronomy, California State University, Sacramento, 6000 J Street, Sacramento, CA 95819-6041, USA
[5] School of Physics and Astronomy, University of Exeter, Stocker Road, Exeter, EX4 4QL, UK
[6] Observatorio Astronómico Nacional (OAN, IGN), Calle Alfonso XII 3, 28014 Madrid, Spain
[7] Max-Planck-Institut für Radioastronomie, Auf dem Hügel 69, 53121 Bonn, Germany
[8] Centre for Astrophysics and Planetary Science, University of Kent, Canterbury, CT2 7NH, UK
[9] Max Planck Institute for Astronomy, Königstuhl 17, 69117 Heidelberg, Germany
[10] Departamento de Astronomía, Universidad de Chile, Casilla 36-D, Santiago, Chile
[11] School of Physics and Astronomy, University of Leeds, Leeds LS2 9JT, UK
[12] Armagh Observatory and Planetarium, College Hill, Armagh, BT61 9DB, UK
[13] Space Science Institute, 4765 Walnut St. Suite B, Boulder CO 80301, USA
[14] School of Science and Technology, University of New England, Armidale NSW 2351, Australia
[15] National Astronomical Observatories, Chinese Academy of Sciences, A20 Datun Road, Chaoyang District, Beijing 100101, PR China

Received 23 December 2022 / Accepted 11 May 2023

ABSTRACT

Context. Filamentary structures in the interstellar medium are closely related to star formation. It is possible that the dense gas mass fraction (DGMF) or clump formation efficiency in large-scale filaments determine whether or not they end up hosting star formation activity.
Aims. We aim to automatically identify large-scale filaments, as well as characterizing them, investigating their association with Galactic structures, and studying their DGMFs.
Methods. We used a modified minimum spanning tree (MST) algorithm to chain parsec-scale ^{13}CO clumps previously extracted from the Structure, Excitation, and Dynamics of the Inner Galactic InterStellar Medium (SEDIGISM) survey. The MST connects nodes in a graph such that the sum of edge lengths is at a minimum. A modified MST also ensures the velocity coherence between nodes, so that the identified filaments are coherent in position-position-velocity (PPV) space.
Results. We generated a catalog of 88 large-scale (>10 pc) filaments in the inner Galactic plane (with $-60° < l < 18°$ and $|b| < 0.5°$). These SEDIGISM filaments are larger and less dense than MST filaments previously identified from the Bolocam Galactic Plane Survey (BGPS) and the APEX Telescope Large Area Survey of the Galaxy (ATLASGAL). We find that eight of the filaments run along spiral arms and can be regarded as the "bones" of the Milky Way. We also found three bones associated with the Local spur in PPV space. By compiling 168 large-scale filaments with available DGMF across the Galaxy, namely, an order of magnitude more than previously investigated, we find that DGMFs are not correlated with Galactic location. We also find that bones have higher DGMFs than other filaments.

Key words. stars: formation – catalogs – ISM: clouds – ISM: molecules – Galaxy: structure – ISM: structure

1. Introduction

The interstellar medium (ISM) has a highly filamentary nature over a broad range of scales (e.g., Andre et al. 2010; Wang et al. 2015; Li et al. 2016; Arzoumanian et al. 2019; Schisano et al. 2020; Palmeirim et al. 2013; Soler et al. 2022) and such filaments may play a vital role in star formation (e.g., Liu et al. 2012, 2016; Peretto et al. 2013, 2014; Yuan et al. 2018; Pillai et al. 2019; Zhang et al. 2019; Xu et al. 2023; Zhang et al. 2023). Theoretical works on filamentary structures can be traced back to Ostriker (1964), who employed a semi-analytic model to characterize an idealized infinite isothermal cylinder under hydrostatic equilibrium. Early observations of filaments, limited by resolution and sensitivity, were focused mainly on nearby regions such as Taurus (Schneider & Elmegreen 1979). The Herschel Space Observatory (Pilbratt et al. 2010) with a higher sensitivity, spatial dynamic range, and angular resolution revolutionized the detailed study of filaments and revealed the ubiquity of filamentary structures throughout the ISM both near (e.g., Andre et al. 2010; Arzoumanian et al. 2011) and far (e.g., Molinari et al. 2010; Wang et al. 2015).

Open Access article, published by EDP Sciences, under the terms of the Creative Commons Attribution License (https://creativecommons.org/licenses/by/4.0), which permits unrestricted use, distribution, and reproduction in any medium, provided the original work is properly cited.
This article is published in open access under the Subscribe to Open model. Subscribe to A&A to support open access publication.

Among the different identified filamentary structures, the large-scale (80 pc) filament seen as a chain of infrared dark clouds (IRDC) known as "Nessie" was first reported by Jackson et al. (2010). Follow-up observations of Nessie in a CO emission line have revealed that it is potentially part of a larger 430 pc structure in the position-position-velocity (PPV) space lying close to the physical Galactic mid-plane (Goodman et al. 2014). The latter suggests that the Nessie IRDC may be a dense "spine" or "bone" of a section of the Scutum–Centaurus Arm. Since then, the existence of many more large-scale massive filaments has been discerned. Their lengths are tens to hundreds of parsecs with masses of up to the order of 10^6 $M_\odot$. These filaments might be formed by large-scale phenomena such as galactic shear, shock in spiral arms, and supernova (SN) feedback (e.g., Smith et al. 2014, 2020; Li et al. 2022; Duarte-Cabral & Dobbs 2016). Several systematic studies of large-scale filaments have been conducted in the past (Ragan et al. 2014; Wang et al. 2015, 2016; Abreu-Vicente et al. 2016; Zucker et al. 2015; Colombo et al. 2021; Ge & Wang 2022). The filaments have been identified in across variety of wavelengths, from the near-infrared, mid-infrared, far-infrared to the submillimeter. Most of these filaments have been detected in Galactic plane unbiased surveys, but they are usually broken into smaller structures by the finding algorithms of those studies (e.g., Schisano et al. 2014, 2020; Koch & Rosolowsky 2015; Li et al. 2016; Mattern et al. 2018). The first identifications of such large-scale filaments were done mostly by eye (Ragan et al. 2014; Wang et al. 2015; Zucker et al. 2015; Abreu-Vicente et al. 2016), but more recently, more automated approaches have recently been developed. For instance, Wang et al. (2016), Ge & Wang (2022) adopted the minimum spanning tree (MST) to automatically identify filaments by "chaining" dense parsec-scale clumps. Colombo et al. (2021) used a dendrogram analysis (Rosolowsky et al. 2008) to isolate coherent structures and then consider long elongated "trunks" of the dendrogram as large-scale filaments. Zucker et al. (2018) analyzed the properties of large-scale filaments in the inner Galaxy from different surveys homogeneously and classified them into sub-samples that may indicate different formation mechanisms or histories. Zhang et al. (2019) also studied large-scale filaments homogeneously, focusing on star-forming content and found that the star formation rate (SFR) surface density and the star formation efficiency (SFE) in large-scale filaments are similar to what is found in molecular clouds in general. In addition to filament catalogs, there are also studies based on individual large-scale filaments such as Orion (e.g., Johnstone & Bally 1999), Taurus L1495 filament (e.g., Schmalzl et al. 2010), Musca filament (e.g., Cox et al. 2016), and other large-scale filamentary clouds or IRDCs (e.g., Battersby et al. 2014; Wang et al. 2014; Du et al. 2017; Sokolov et al. 2017, 2018, 2019; Liu et al. 2018; Watkins et al. 2019; Tang et al. 2019; Lin et al. 2020; Guo et al. 2022; Veena et al. 2021; Clarke et al. 2023; Chen et al. 2023).

Star formation takes place in dense regions of molecular clouds known as clumps. The fraction of dense gas in the molecular clouds has been linked to the SFR (e.g., Lada et al. 2012). This fraction is often referred to as the dense gas mass fraction (DGMF) or clump formation efficiency (CFE). The DGMF does not show any specific correlation with the total cloud mass, and the lack of dense gas will cause inefficiency of star formation (Battisti & Heyer 2014). Eden et al. (2013) found that the CFE of molecular clouds in the Milky Way shows no difference between the inter-arm and spiral-arm regions. They further inferred that outside the Galactic center region, Galactic-scale structures do not play a significant role in the formation of dense, potentially star-forming structures within molecular clouds. In contrast, Torii et al. (2019) found that the molecular clouds within spiral arms have a higher fraction of dense gas than inter-arm clouds. For filaments, from the study of 163 large-scale filaments, Ge & Wang (2022) found that DGMF in the spiral arms has no significant distinction from inter-arm filaments. Zhang et al. (2019) also found that star formation activity per gas mass in spiral arm and inter-arm environments are similar. However, some other studies have found that the DGMFs of filaments in spiral arms are higher than those of inter-arm ones (Ragan et al. 2014; Abreu-Vicente et al. 2016). These authors suggest that star-formation activity in large-scale filaments depends on their location with respect to the spiral arms. We note that these results are derived based on small numbers of filaments (9 and 16) and should be taken with caution, as pointed out by the authors (Ragan et al. 2014; Abreu-Vicente et al. 2016). The DGMFs of large-scale filaments are also found to have similar values compared to those in nearby galaxies (Wang et al. 2020b).

A MST is a unique set of straight lines ("edges") connecting a given set of points ("nodes") without closed loops, such that the sum of the edge lengths is minimum. Thus far, MST has been widely used in astrophysics to find large-scale distribution of galaxy or galaxy clusters, and it has also been used to find filamentary features (e.g., Barrow et al. 1985; Adami & Mazure 1999; Doroshkevich et al. 2004; Colberg 2007; Park & Lee 2009; Alpaslan et al. 2014; Naidoo et al. 2020; Pereyra et al. 2020). In addition, MST has been used to identify star clusters (e.g., Cartwright & Whitworth 2004; Schmeja & Klessen 2006; Gutermuth et al. 2009; Wu et al. 2017) and quantify core separations and mass segregation (e.g., Sanhueza et al. 2019; Dib & Henning 2019). The main advantage of the MST adopted by Wang et al. (2016) is that it considers an additional dimension: the velocity. Therefore, it is a clustering process in 3D (PPV) space, rather than a procedure purely based on 2D morphological characteristics. Using the MST method, Wang et al. (2016) identified and characterized 54 large-scale velocity-coherent filaments in the Bolocam Galactic Plane Survey (BGPS), while Ge & Wang (2022) built a catalog of 163 filaments in the APEX Telescope Large Area Survey of the Galaxy (ATLASGAL). These works have greatly increased the number of known large-scale filaments and, more importantly, they have introduced a physically driven definition of filaments (Wang et al. 2016), making it possible for statistically significant results to be derived, for instance: an association with Galactic spiral arms, dense gas fraction, and other parameters. Both BGPS and ATLASGAL are based on the dust continuum and thus primarily trace relatively dense gas. The recently published SEDIGISM cloud catalog extracted from ^{13}CO emission (Duarte-Cabral et al. 2021) provides us with high-quality nodes for MST. As such, we can search for more diffuse large-scale filaments with comparatively lower densities. Moreover, the survey includes the region near the Galactic center (Galactic longitude $|l| < 5°$), which is not included in the works of Wang et al. (2016) and Ge & Wang (2022), due to the coverage of the input PPV catalogs they used.

In this paper, we identify large-scale filaments in the Galactic plane, investigate their association with Galactic structures, and study their DGMFs. The paper is structured as follows. We describe the data and methodology that we used to identify large-scale filaments in Sect. 2. In Sect. 3, we present our results, including the physical properties of large-scale filaments and statistics. We also compare our SEDIGISM filaments with two other MST filament catalogs (from BGPS and ATLASGAL) and other previously known large-scale filaments. Then in Sect. 4, we investigate the association between filaments and Galactic spiral arms and examine DGMFs of filaments in different

Galactic locations as well. Finally, we summarize our results in Sect. 5.

2. Data and method

2.1. SEDIGISM molecular clouds

The SEDIGISM survey used the APEX telescope to map the Galactic plane in $300° < l < 18°$ with $|b| \leq 0.5$ continuously and then a small region around W43 ($29° < l < 31°$ with $|b| \leq 0.5$) in several molecular transitions, including ^{13}CO(2–1) and C^{18}O(2–1), with an angular resolution of 30″ (Schuller et al. 2017, 2021). Using the ^{13}CO(2–1) emission in the SEDIGISM spectral-line survey, Duarte-Cabral et al. (2021) extracted the molecular cloud population with a large dynamic range in spatial scales. They used the Spectral Clustering for Interstellar Molecular Emission Segmentation (SCIMES) algorithm (Colombo et al. 2015, 2019) and compiled a cloud catalog with a total of 10663 molecular clouds. In brief, they first constructed dendrograms[1] from the preprocessed[2] SEDIGISM data cubes. Secondly, they identified gas clusters (cloud candidates) within the dendrograms using the SCIMES algorithm. Thirdly, they handled clouds in overlapping regions and removed spurious sources. Although they also included a clustering analysis, the lack of large nearby clouds ($d < 2.5$ kpc) indicates that they might be breaking nearby clouds into smaller substructures. In addition, despite the fact that Neralwar et al. (2022) classified these clouds as filaments and nonfilaments, large filaments are found to be outliers. This may be due to the noise in the long filaments. That is to say that if a filament itself falls below the noise threshold in sections (that means this long filament is divided into pieces by several noisy parts), it is not continuous in emission. Then it is not part of the same dendrogram structure and, therefore, SCIMES could never connect the two sections together. Limited by the data in this why, if we intended to study large filamentary clouds, an alternative method would be required. The MST method described in the next section provides us with a way to deal with this limitation. In the SEDIGISM cloud catalog, most of the clouds (84%, or 8945/10663) contain only a single dendrogram leaf[3]. A chain of such clouds (or leaves) in PPV space could be a structure on a grander scale. This catalog of SEDIGISM clouds, containing only one leaf (hereafter "SEDIGISM leaves"), is an excellent data set for searching velocity-coherent filaments.

2.2. MST filament identification

We identified large-scale velocity-coherent filaments using the modified minimum spanning tree algorithm[4] (Wang et al. 2016). A spanning tree is defined as a network connecting all nodes on a graph. An MST connects all nodes so that the sum of edges is minimal and there are no loops on it. In the modified MST by Wang et al. (2016), an additional dimension, velocity, is considered. When a node is to join the tree, it will be accepted only when it has a velocity similar to a nearby node in the tree. We consider the SEDIGISM leaves described in Sect. 2.1 as nodes in the algorithm. The criteria for MST matching and filament selection follow Wang et al. (2016), Ge & Wang (2022) and are as follows: (1) the accepted MST must contain at least five SEDIGISM leaves: $N \geq 5$; (2) only edges shorter than a maximum length (cut-off length) can be connected ($\Delta L < 0.^{\circ}1$); (3) for any two leaves to be connected, the difference in line-of-sight velocity (matching velocity Δv) must be less than 2 km s^{-1}; (4) linearity $f_L > 1.6$. Here, linearity is defined to quantify the degree of similarity between the target shape with a straight line shape; and (5) projected length (sum of edges) $L_{\rm sum} \geq 10$ pc. We note that we only focus on large-scale filaments in this work.

The value for N refers to the pruning level of MSTs in Park & Lee (2009) and Pereyra et al. (2020). In their work, when a branch of an MST has fewer than five nodes, it is thought to be a minor branch and should be removed from the tree. The cut-off length is chosen because the observed angle for a filament with a length of 10 pc at a distance of 5 kpc is about $0.^{\circ}1$. The velocity difference between the two ends of a filament has an order of 1 km s^{-1} if we treat the velocity gradient as 0.1 km s^{-1} pc^{-1}. This order of velocity gradient is estimated by averaging the global velocity gradients of the filaments from several large-scale filament catalogs (Ragan et al. 2014; Wang et al. 2015; Zucker et al. 2015; Abreu-Vicente et al. 2016). We tested 1, 2, 3, and 5 km s^{-1} for matching velocity. We find that 1 km s^{-1} is too strict to connect leaves. Results obtained for 2, 3, and 5 km s^{-1} do not vary too much. This is reasonable considering the low possibility that a physically isolated source is observed exactly within a structure. Then we chose the relatively strict matching velocity of 2 km s^{-1}. Linearity is the ratio between the spread (standard deviation) of leaves along the major axis and the spread perpendicular to the major axis. To define the major axis of a filament, we plot all the leaves belonging to this filament in the projected sky (Galactic longitude as x and Galactic latitude as y) and fit a line with principle component analysis (PCA, Pearson 1901) as the major axis of this filament. We slightly increased the critical linearity compared to Wang et al. (2016) and Ge & Wang (2022) (1.5), where a few MSTs are more likely to be a collection of clumps within a larger cloud-like environment. A collection of clumps displays a lower linearity and aspect ratio than a filament. These dense structures have the potential to develop within the network of filaments within large molecular clouds and can grow in size by preferentially gathering gas from the greater gravo-turbulent molecular cloud environment rather than forming through sausage instability of a single large-scale filament (Zucker et al. 2018). Identifying them is still useful, but this is beyond the scope of this paper. We tested various critical linearity values and found that 1.6 is the best value to remove collections of leaves and, at the same time, to avoid getting rid of real filaments.

2.3. Large-scale filaments in the SEDIGISM cloud catalog

In Sect. 2.2, we describe how to identify large-scale filaments using the SEDIGISM leaves. However, there are also several clouds (16%, or 1718/10663) in the SEDIGISM cloud catalog (Duarte-Cabral et al. 2021) that contain more than one dendrogram leaf. We selected large elongated objects from these

[1] Using ASTRODENDRO based on the original IDL procedures from Rosolowsky et al. (2008).
[2] Includes an enhancement of the signal-to-noise ratio of the data set by smoothing the data in velocity and mask the datacubes using the local noise level.
[3] Before the clustering analysis of SCIMES, the dendrograms are constructed from the SEDIGISM datacubes. The dendrogram is made up of three different kinds of structures: the trunk, which is at the bottom of the hierarchy (i.e., it has no parent structure) and contains all branches and leaves: (1) branches, which split into multiple substructures; and (2) leaves, which are at the top of the hierarchy and contain no substructure because they are connected to local peaks of emission.
[4] The code is available at Wang & Ge (2021), https://ascl.net/2102.002

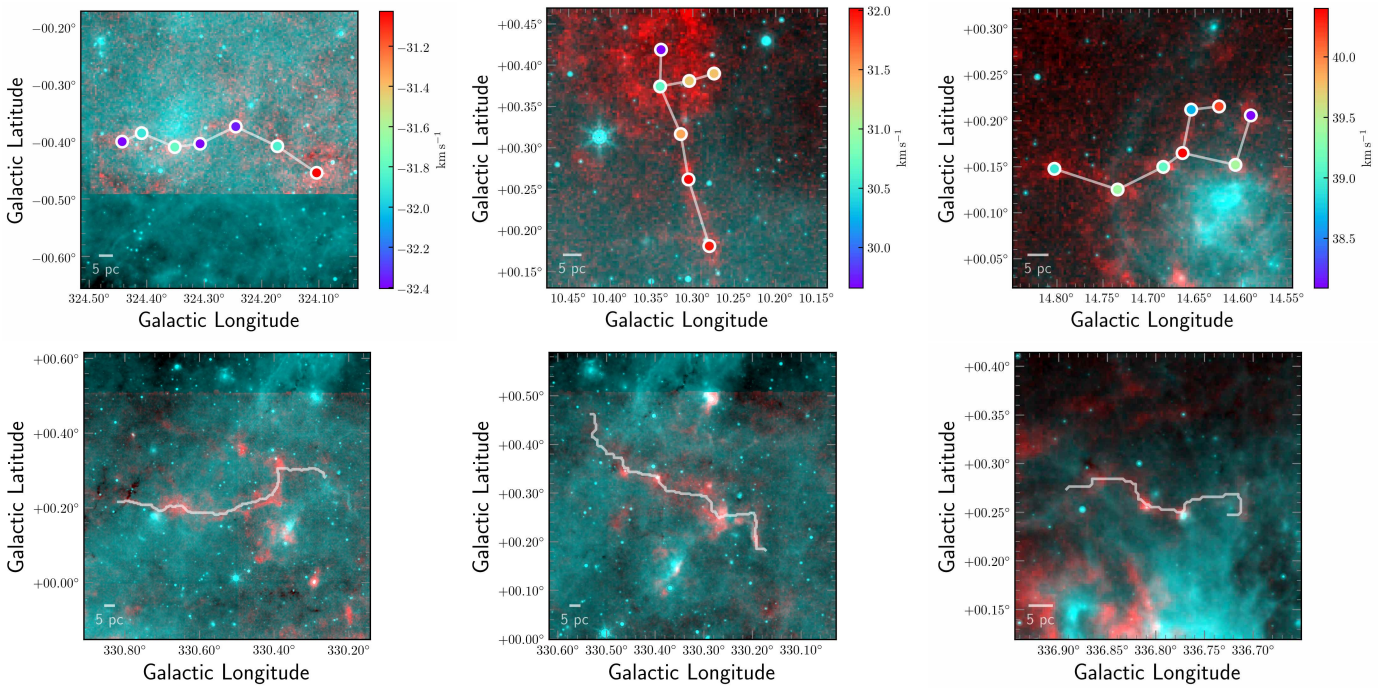

Fig. 1. Two-color composite images of six example large-scale filaments. In all panels, red shows integrated ^{13}CO(2–1) emission in a linear scale, and cyan represents MIPSGAL mid-infrared 24 μm emission (Carey et al. 2009) in a logarithmic scale. The top three panels show filaments identified from SEDIGISM leaves with the MST approach (M7, M45, and M51, respectively). The color-coded circles denote leaves in filaments with different velocities and the white line segments are the edges. The color bars show the radial velocities of the leaves. The bottom three panels show large elongated filaments selected from the SEDIGISM cloud catalog (S62, S63, and S69, respectively). White curves are their medial axis. Two-color composite images for all the 88 filaments are shown in Appendix E.

clouds to enlarge our filament sample. Specifically, a cloud can be regarded as a large-scale filament only when it satisfies the following conditions: (1) the cloud must contain at least five dendrogram leaves: $N \geq 5$; (2) the aspect ratio is >3.5, which is the ratio between the major and minor axis; and (3) the medial axis length $l_{\rm MA} \geq 10$ pc.

The criteria are chosen to be identical to those of the MST analysis when possible. The required number of nodes is the same as what we do in the MST. The aspect ratio is derived from the second moment of the emission in 2D, weighted by the intensity (Duarte-Cabral et al. 2021). The aspect ratio threshold is chosen because if we apply this value to MST, it will select similar structures as our linearity threshold does. That is, when we replace the criterion linearity >1.6 with an aspect ratio >3.5 for the MST, most of the filaments retain. The skeleton of a cloud is derived from the medial axis transform, which calculates the position of the skeleton by computing the minimum distance of each pixel in the structure to the pixel outside of it. The result of this method is reducing a structure to a single-pixel-wide skeleton. The medial axis is the longest-running skeleton along the 2D-projected cloud mask. It is farthest away from the external edges (see Fig. 5 in Duarte-Cabral et al. 2021, for an example). As we are interested in the large-scale filaments, the length threshold is 10 pc, the same as that for the MST filaments. J-plot is a method to classify pixelated structures into different morphology (Jaffa et al. 2018). Two J moments (J_1 and J_2) are calculated with principal moments of inertia along the two principal axes of the structures. Neralwar et al. (2022) used a J-plot to classify clouds into three types: centrally concentrated disks (cores) with $J_1 > 0$ and $J_2 > 0$; elongated ellipses (filaments) with $J_1 > 0$ and $J_2 < 0$; and rings (limb-brightened bubbles) with $J_1 < 0$ and $J_2 < 0$. We find all of the clouds selected following the above three criteria are also classified as filaments by Neralwar et al. (2022).

3. Results

We identified 55 large-scale filaments through SEDIGISM leaves with the MST approach (method described in Sect. 2.2) and selected 33 large elongated filaments from the SEDIGISM cloud catalog (criteria described in Sect. 2.3). These two samples compose our large-scale filament catalog. In summary, this large-scale filament catalog contains 88 filaments in the inner Galactic plane (with $-60° < l < 18°$ and $|b| < 0.^\circ5$). The two-color composite images of some of the filaments are shown in Fig. 1. The CO emission is from SEDIGISM (Schuller et al. 2021) and the 24 μm emission from Carey et al. (2009) is used to examine whether a filament is infrared dark. The Multi-band Imaging Photometer Galactic Plane Survey (MIPSGAL) is an infrared survey with a resolution of 6″ at 24 μm.

To discern which filaments are new identifications, we compared our catalog to the MST filaments from BGPS (Wang et al. 2016), ATLASGAL (Ge & Wang 2022), and other previously known large-scale filaments. We find that 11 of our filaments are the same or overlap with those from ATLASGAL and only one of our filaments has overlap with a filament from BGPS, as listed in the last column of Table A.1. The small number of our filaments overlapping with BGPS filaments is due to the survey coverage difference, meaning that most of our filaments are identified in the Southern sky ($-60° < l < 18°$) while BGPS filaments are in the northern sky ($7.^\circ5 < l < 194°$). In the common coverage of SEDIGISM and ATLASGAL ($-60° < l < 18°$ and $-0.^\circ5 < b < 0.^\circ5$), 77 SEDIGISM filaments are not identified

in the ATLASGAL filament catalog. The main cause for this may be the different tracer that is used. ATLASGAL clumps are extracted from 870 μm dust continuum which traces relatively dense regions, while SEDIGISM clouds are extracted from ^{13}CO emission, which can trace more diffuse, lower density structures. As a result, some filamentary structures that are not conspicuous in the dust continuum can be identified from ^{13}CO emission. Similarly, Duarte-Cabral et al. (2021) found that only a small portion (∼16%) of SEDIGISM clouds are associated with dense clumps as traced by ATLASGAL.

As for the comparison to other known large-scale filaments, 13 of our filaments have overlap with Milky Way bones (Zucker et al. 2015; Jackson et al. 2010) and giant molecular filaments (GMFs, Abreu-Vicente et al. 2016), based on the reanalysis and terms from Zucker et al. (2018). The corresponding associations and references are listed in the last column of Table A.1. In the common Galactic longitude range ($-60° < l < 18°$) where Milky Way bones, GMFs, and our SEDIGISM filaments reside, there are 14 Milky Way bones or GMFs. Eight of them are identified in our SEDIGISM large-scale filament catalog (though three of them are split into multiple filaments). Following a comparison with BGPS filaments, ATLASGAL filaments, and other known large-scale filaments, we find 66 of our filaments are newly identified large-scale filaments.

3.1. Galactic locations and physical properties

The physical properties of the 88 filaments are shown in Table A.1. Filaments with ID M1-M55 are those identified from SEDIGISM leaves via MST, while S56-S88 correspond to filaments selected from the SEDIGISM cloud catalog (see Sect. 2.3 for selection criteria). Some of the physical properties are derived differently for filaments identified through leaves with MST (M1-M55) and filaments selected from SEDIGISM clouds (S56-S88). If so, this physical property will be described individually for the two categories. Apart from a small portion of clouds associated with masers, the distance values for most clouds in the SEDIGISM cloud catalog are kinematic distances determined after solving for distance ambiguities (Sect. 4 in Duarte-Cabral et al. 2021). The distances of filaments listed in Col. (6) are the median of leaf distances for M1-M55, while they are taken from the SEDIGISM cloud catalog for S56-S88. For M1-M55, the aspect ratio in Col. (13) is the ratio of the area between the circle enclosing the filament and the concave hull (the minimum-area concave polygon that contains all the leaves in the MST). For an approximately elliptical distribution, f_A is very similar to the aspect ratio of the ellipse when the number of nodes is large (Gutermuth et al. 2009). For S56-S88, the aspect ratio is the ratio between the major and minor axis of the ellipse. For M1-M55, $|\theta|$ in Col. (17) is derived from PCA (orientation of the major axis described in Sect. 2.2). For S56-S88, $|\theta|$ is the position angle of the major axis, with 0 being along the l axis.

DGMFs for S56-S88 are taken from Urquhart et al. (2021) with an uncertainty of a factor of 2.5 (or 0.45 dex). They take the ATLASGAL mass of the clumps coincident with a SEDIGISM cloud in position and velocity as the value of the dense mass, and their DGMF is defined as DGF = $\Sigma M_{\rm clump}/M_{\rm cloud}$. Material traced by ATLASGAL has column densities about 15 times higher than clouds traced by SEDIGISM (Urquhart et al. 2021). As for M1-M55, we follow a similar approach. That is, dense gas mass can be calculated directly from the DGMFs of the leaves. We take the sum of the dense gas mass of leaves in a filament as the dense gas mass of this filament ($\sum_{i=1}^{N} M_i \cdot {\rm DGF}_i$, where N is the number of leaves the filament contains). With this dense mass and total mass of filaments ($\sum M_{\rm leaves}$), DGMFs for filaments M1-M55 are calculated. The DGMFs are listed in Col. (18) of Table A.1. Filaments with a DGMF of "-" correspond to those that do not host any ATLASGAL clumps. The statistics of the filament properties are shown in the last seven rows of Table A.1, including minimum, maximum, median, mean, standard deviation, skewness (S), and kurtosis (K).

3.2. Distribution of Galactic locations and physical properties

Histograms of the Galactic locations and physical properties of filaments are shown in Fig. 2. Panels a–k show their Galactic longitudes and latitudes, local standard of rest (LSR) velocities, distances, total mass, lengths (sum of edges), line mass, column density, Galactic height, Galactocentric radius, and orientation angles in the projected sky, respectively. For comparison, the properties of filaments from two other categories of MST filaments are also plotted, where red histograms show MST filaments identified through BGPS sources (hereafter, "BGPS filaments", Wang et al. 2016) and green histograms denote MST filaments identified through ATLASGAL clumps (hereafter, "ATLASGAL filaments", Ge & Wang 2022).

For the Galactic longitude distribution shown in Fig. 2a, there is a peak around $l = 335°$. That is because the distribution of Galactic longitude for leaves (SEDIGISM clouds containing only one dendrogram leaf, which we used to identify filaments) also peaks around that longitude, and filaments tend to be found in the region where leaves are crowded. Meanwhile, ATLASGAL filaments also peak around this Galactic longitude. The peak is found in Mattern et al. (2018) as well. Their sample is selected from ATLASGAL filaments (Li et al. 2016) identified through DisPerSE with a median length of about 10 pc. They attribute the decrease in the number of filaments towards the Galactic center to the difficulty in identifying filaments in confused structures and the decrease in the number towards the outer Galaxy to the lack of dense molecular clouds. In Fig. 2b, we can see that the distribution of Galactic latitudes for filaments in this work is less spread (with a standard deviation of 0.26°, while this value for BGPS filaments and ATLASGAL filaments are 0.38° and 0.36°, respectively) as a result of the relatively narrow Galactic latitude range for SEDIGISM data. No filaments are found in this work in the velocity range between 50 km s^{-1} and 130 km s^{-1} (see Fig. 2c). Five filaments have a velocity larger than 130 km s^{-1}, and they are all close to the Galactic center with Galactic longitudes $0° < l < 10°$. This distribution is also consistent with the velocity of SEDIGISM clouds (see Fig. 1 in Duarte-Cabral et al. 2021). As seen in Fig. 2d, unlike BGPS and ATLASGAL where the majority of filaments are relatively nearby (<5 kpc), filaments in this work have distances spread over a wide range.

As shown in Fig. 2e, the total mass of filaments in this work ranges from 10^3–10^6 $M_\odot$. The length (sum of edges) distribution of the filaments in this work is shown in Fig. 2f and has a longer tail than the other two samples. We see that 17% of the filaments in this work have a length larger than 100 pc, while those for BGPS and ATLASGAL filaments are 2 and 4%, respectively. The average length of filaments in this work (65.5 pc) is also much larger than the other two (35.7 pc for BGPS and 38.7 pc for ATLASGAL). This is because SEDIGISM leaves are extracted from ^{13}CO emission, which traces relatively diffused structures with a median effective radius of 2.0 pc, while BGPS sources and ATLASGAL clumps are more condensed continuum sources both with mean or median effective radius of about 0.7 pc. For the same reason, the line mass and column density of the

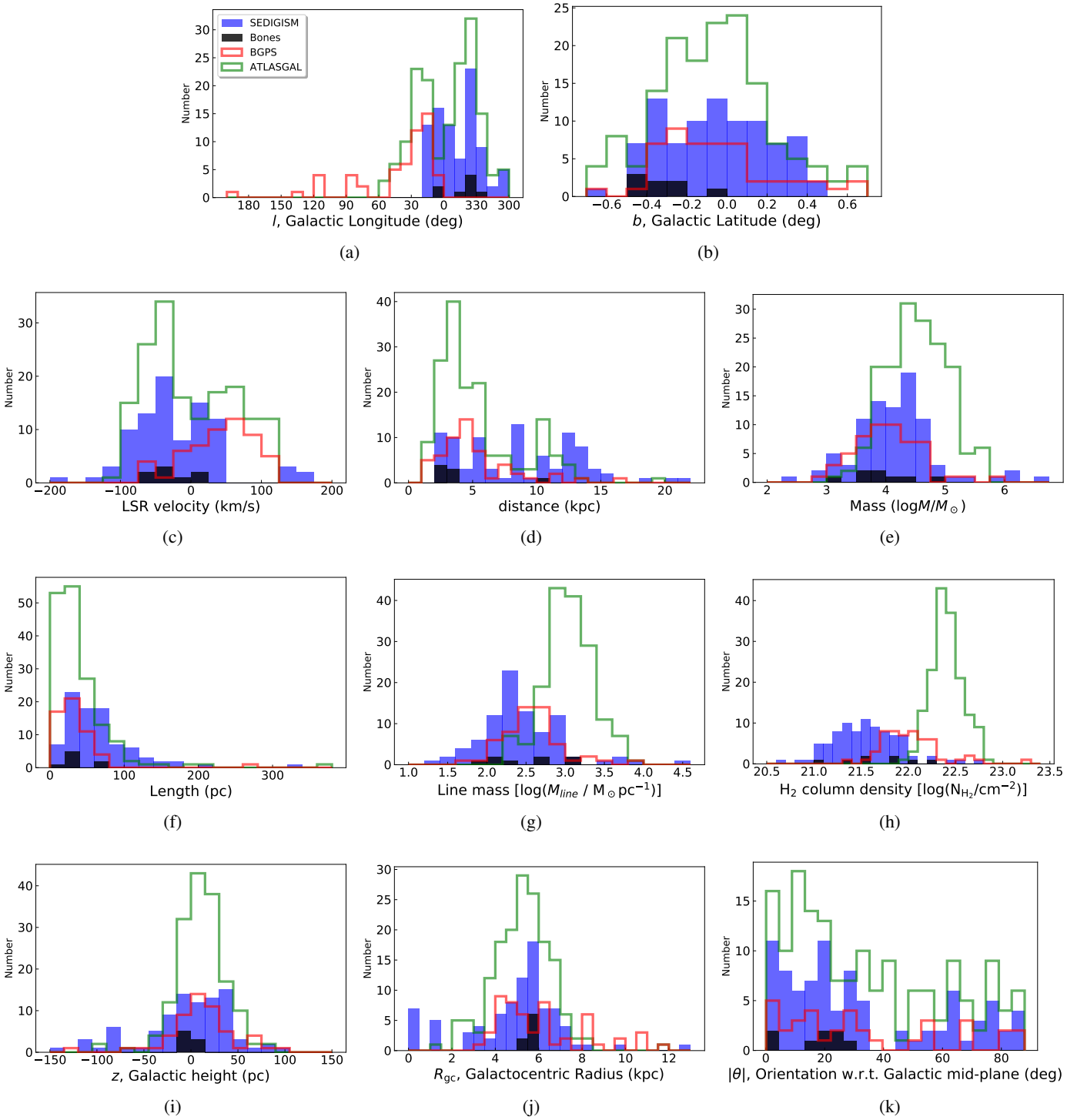

Fig. 2. Histograms showing physical properties of the 88 SEDIGISM filaments (blue: this work), as compared to the 54 BGPS filaments (red, Wang et al. 2016) and the 163 ATLASGAL filaments (green, Ge & Wang 2022). Panels a–k show the distribution in Galactic longitude and latitude, LSR velocity, distance, total mass, length (sum of edges), line mass, column density, Galactic height (distance from the Galactic mid-plane), Galactocentric radius, and orientation angle, respectively. The "bones" discussed in Sect. 4.1 are plotted in black.

filaments in this work is smaller than the other two as shown in Figs. 2g and h. Zucker et al. (2018) also found that one class of large-scale filaments called "GMFs" (Ragan et al. 2014; Abreu-Vicente et al. 2016) whose boundaries are derived from ^{13}CO are shown to have lower column densities than other classes of filaments.

Regarding the Galactic height shown in Fig. 2i, there are more filaments with positive z than negative (skews towards the negative values with $S = -0.8$). That does not mean that large-scale filaments prefer to be located above the Galactic mid-plane. The reason is that the Galactic plane survey is centered at $b = 0°$, while the true Galactic mid-plane has a negative Galactic latitude due to our Sun being located above the plane (Ragan et al. 2014). The Galactocentric radius shown in Fig. 2j is more centrally peaked compared to a normal distribution (with Kurtosis, $K = 1.9$). There are also some filaments near the

Galactic center, where no BGPS or ATLASGAL filaments exist (limited by the coverage of the relevant PPV catalogs).

In Fig. 2k, we can see that the majority of filaments are either parallel ($|\theta| < 30°$, parallel end) or perpendicular ($|\theta| > 60°$, vertical end) with respect to the Galactic mid-plane. This preference does not occur in BGPS (orientations for BGPS filaments are recalculated with PCA) or ATLASGAL filaments. Most of the observed large-scale filaments tend to be more parallel to the Galactic mid-plane than expected randomly (Zucker et al. 2018). This is also the case for our SEDIGISM filaments as ~60% of them distribute in the parallel end. Using a sample of large-scale filaments extracted from a simulation of a Milky Way-like galaxy, Zucker et al. (2019) find that without feedback in the simulations, it is unsurprising that every filament in the sample forms aligned with the gravitational mid-plane of the simulation. When SN feedback exists in the simulation, the shells developed from SN remnant collide to form large filamentary clouds (Joung & Mac Low 2006). Interaction between large-scale filaments and SN bubbles has also been observed (Li et al. 2013, 2022; Chen et al. 2023). So a portion of our vertical filaments might be a result of SN feedback. Besides, one study of the HI filament (Soler et al. 2022) reported that there is a significant number of vertical HI filaments and SN bubbles beyond the Solar circle in the region of the SEDIGISM survey. But we note that the orientation of the filamentary structures traced by HI is not, in general, inherited by the structures traced by CO (Soler et al. 2021).

4. Discussion

4.1. Large-scale filaments in the Milky Way

4.1.1. Considering the possible "bones" of the Milky Way

Some large-scale filaments have been described as "bones" of the Milky Way since Goodman et al. (2014) reported the first case. Zucker et al. (2015) established a set of criteria for large-scale filaments to be considered as bones, which was later refined by Wang et al. (2016). Ge & Wang (2022) defined three major aspects that can be adopted to judge whether a filament is a bone, namely, it is: (1) parallel to the Galactic plane, to within 30°; (2) lies very close to the Galactic mid-plane, $|z| \leq 20$ pc; and (3) the flux-weighted LSR velocity is within ± 5 km s^{-1} from the centers of spiral arms. To investigate the third criterion, we employed the spiral arm model from Taylor & Cordes (1993) as updated by Cordes (2004). We did not choose another widely used spiral arm model such as that of Reid et al. (2019) because most high-mass star-forming regions used to fit the model are in the first and second Milky Way quadrants, while the majority of our filaments reside in the fourth quadrant where their spiral arm model is determined by extrapolation. The Reid et al. (2019) spiral arm model and the more recent spiral arm model by Hou (2021) were used to test the influence in our results of the chosen model, as described in Appendix B.

To investigate the association between large-scale filaments and spiral arms, we examine whether our filaments are close to spiral arms in the position-velocity (PV) space. The x and y positions of Taylor & Cordes (1993) arms shown in the bottom panel of Fig. 3 are converted into l and v using a rotation curve from Reid et al. (2019). Solar position and velocity are also from Reid et al. (2019), which are 8.15 kpc and 236 km s^{-1}. The longitude-velocity (lv) plot of filaments and spiral arms is shown in the top panel of Fig. 3. Spiral arm loci (belts) with various colors represent arms in Taylor & Cordes (1993) model, and widths are 10 km s^{-1}. Black circles denote our filaments. If the center of a circle falls within one of the belts, it means the corresponding filament is associated with this arm in PV space. We found that 44 (out of a total of 88) of the filaments are arm filaments, and their PV-associated arms are listed in Col. (20) of Table A.1. Most arm filaments (25/44) are associated with the Scutum-Centaurus arm. This preference in the association is also found by Abreu-Vicente et al. (2016), Zucker et al. (2018), and Mattern et al. (2018). We cannot eliminate the possibility this might just be a sensitivity effect because the mass of filaments is correlated with distance (the Spearman correlation coefficient is 0.38 with a p-value of 0.0002). It could also be that this is the arm that appears to us mostly in the plane of the sky, which enhances the chance of detecting these large filaments if they are aligned with the arms. Looking through the tangent then these filaments would look a lot less "stretched". Five arm filaments are associated with the Perseus arm, nine with Norma-Outer, and five with Sagittarius-Carina. Our data do not support a grand design spiral pattern, but neither are they opposed to this pattern – our aim is simply to show this optimistic presumption of a spiral structure.

For the filaments associated with spiral arms in the PV space, we consider the remaining two criteria (roughly parallel and close to Galactic mid-plane) and find that eight of them satisfy both of them. Therefore, eight of our filaments are bones according to the three criteria and they are listed in Col. (20) of Table A.1. Their physical properties are shown as black bars in Fig. 2, which do not stand out compared to other filaments. Our eight bones are smaller and less massive than those identified in Abreu-Vicente et al. (2016). Compared to bones reported in Ge & Wang (2022), our bones are less massive.

4.1.2. Association with spurs

Besides the main spiral arms, some substructures named "spurs" (or "bridges", "branches", or "armlets") have also been observed in our Milky Way (e.g., Sofue 1976; Rickard & Cronyn 1979; Xu et al. 2016). They are much shorter than spiral arms but substantially longer than large-scale filaments. These substructures also occur in simulations and their formation is different for the different spiral arm models, including gravitational instabilities (e.g., Dobbs & Bonnell 2006), magneto-Jeans instabilities (e.g., Kim & Ostriker 2006), wiggle instabilities (e.g., Wada & Koda 2004; Mandowara et al. 2022), and the effect of correlated SN feedbacks (e.g., Kim et al. 2020). Spurs could possibly act as a diagnostic tool regarding the origin of spiral arm structure, with different arm generation mechanisms (such as tidal interactions) producing comparatively strong spurs (Pettitt et al. 2020). A study on the association between spurs and large-scale filaments is helpful for our understanding of large-scale filaments and spiral arms.

We checked whether large-scale filaments are associated with two known spurs. One is a spur identified by Xu et al. (2016) that bridges the Local arm to the Sagittarius arm. It is shown as an orange belt labeled "Local spur" in Fig. 4. The other is a spur between the Sagittarius and Scutum arms mentioned by Reid et al. (2019). It is shown as a purple belt labeled "Scutum spur" in Fig. 4. As seen in the upper panel of Fig. 4, there are two ATLASGAL filaments and one previous large-scale filament lying within the Local spur in the PV space. The two ATLASGAL filaments are shown as orange plus symbols and they are F69 and F70 in Ge & Wang (2022). The one previously identified large-scale filament is shown as an orange triangle and it is G64 from Wang et al. (2015). As shown in the lower panel of Fig. 4, the three filaments are also located close to the Local spur in the face-on view of the Galaxy. In fact,

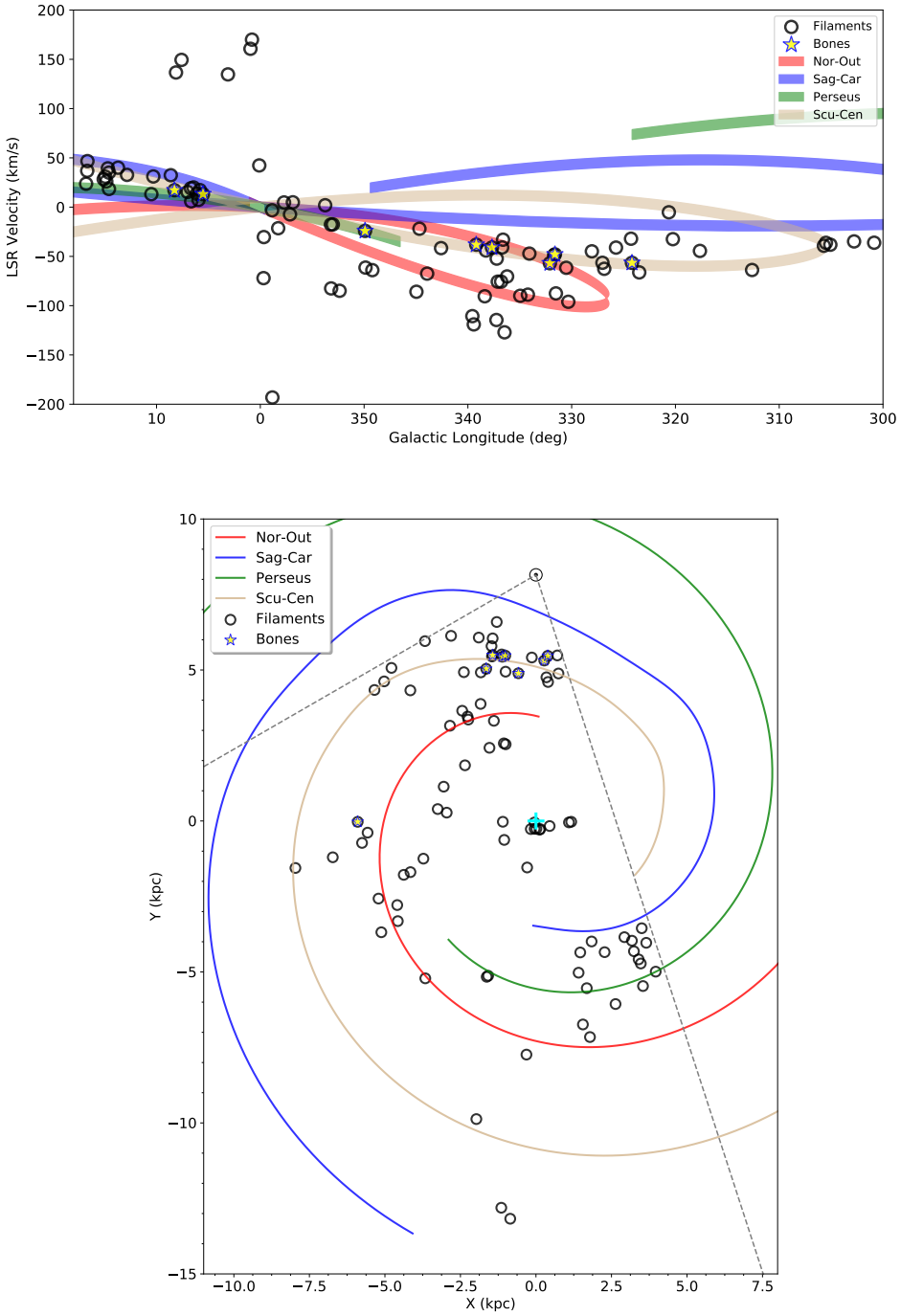

Fig. 3. Distribution of large-scale filaments with respect to spiral arms. The top panel is a longitude–velocity view of filaments and spiral arms. Belts with various colors are arms in Taylor & Cordes (1993) model, and widths are 10 km s^{-1}. Red, brown, blue, and green represent the Norma-Outer, Scutum-Centaurus, Sagittarius-Carina, and Perseus arms, respectively. Black circles denote our filaments and stars are "bones". The bottom panel shows a face-on view of filaments and spiral arms. The cyan plus symbol represents the Galactic center, and grey dashed lines show the data range. The solar symbol ⊙ is plotted at (0, 8.15) kpc (Reid et al. 2019).

the three filaments lie very close to the Galactic mid-plane and satisfy the criteria for bones. So, we suggest that these three filaments are potentially bones of the Local spur. Based on the Local spur CO survey, Kohno et al. (2022) found three large-scale filaments in the Sh 2-86 high-mass star-forming region. The F70 is part of their Filament C. They suggest that these filaments are formed by galactic-scale dynamics such as spiral shocks or shear motions. As for the Scutum spur, there is no filament associated with it.

4.2. Dense gas mass fraction

The DGMF (or CFE) is the dense-clump analog (or precursor) of the SFE and is tightly associated with star formation (e.g., Lada et al. 2012; Eden et al. 2013; Battisti & Heyer 2014). There are two key points to consider when calculating DGMFs. One is to define the dense gas properly and the other is to unify the dense gas mass and the total mass with the same formulation and parameters. The dense gas in this work is determined

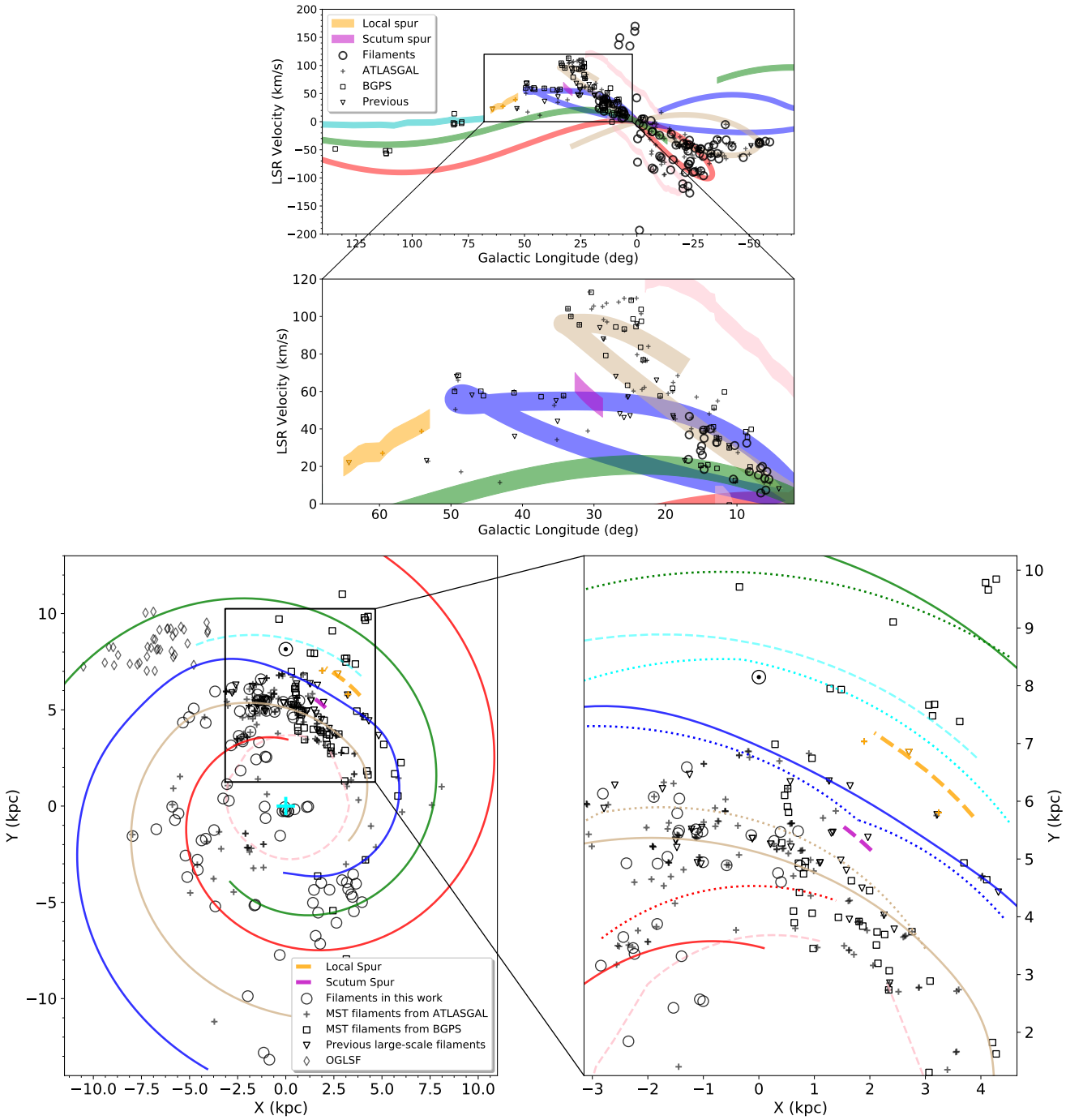

Fig. 4. Large-scale filaments and spurs. Top panel: longitude–velocity view of filaments and spiral arms as well as spurs. Belts with various colors are arms in Taylor & Cordes (1993) model or spurs from Reid et al. (2019) with widths of 10 km s^{-1}. Red, brown, blue, and green represent the Norma-Outer, Scutum-Centaurus, Sagittarius-Carina, and Perseus arms, respectively. The orange belt marks the Local spur and the purple belt is the Scutum spur. Black circles denote our SEDIGISM filaments. Black plus symbols, squares, triangles, and diamonds represent ATLASGAL filaments (Ge & Wang 2022), BGPS filaments (Wang et al. 2016), previously known filaments (Zucker et al. 2018), and outer Galaxy large-scale filaments (OGLSF, Colombo et al. 2021), respectively. Orange marks denote filaments associated with the Local spur. We zoom in on the region around the two spurs. Bottom panel: Face-on view of filaments and spiral arms as well as spurs. The cyan and pink dashed curves represent the Local arm and 3 kpc arm from Reid et al. (2019). Since the zoom-in region is in the solar neighborhood, as a reference, we plot arms from Hou (2021) model as dotted curves. Other symbols follow the convention of the top panel.

as the total mass of ATLASGAL clumps matching a given filament in position and velocity (Urquhart et al. 2021). The DGMF is then the ratio of the dense gas mass to the filament mass as listed in Table A.1. Since the masses of ATLASGAL clump and SEDIGISM clouds are calculated with different dust opacity values, Urquhart et al. (2021) was able to unify them to the same opacity. The ATLASGAL uses 1.85 $cm^2\ g^{-1}$ at 350 GHz as opacity (Schuller et al. 2009), while the SEDIGISM employs CO X factor to convert CO to H_2. The X factor is derived from an opacity of 0.1 $cm^2\ g^{-1}$ at 1200 GHz (Elia et al. 2013). This opacity will be 8.5×10^{-3} $cm^2\ g^{-1}$ at the ATLASGAL frequency. The result of the opacity difference is that the ATLASGAL clump

masses should be multiplied by a factor of 1.61 to match the masses of SEDIGISM clouds (Urquhart et al. 2021). The relating 5σ column density threshold for the ATLASGAL survey should also change from 7.5×10^{21} cm^{-2} to 1.5×10^{22} cm^{-2}. For comparison, the column density sensitivity of SEDIGISM is 0.95×10^{21} cm^{-2}. The advantage of this calculation is that it has a well-defined dense gas mass and the parameters have been calculated following a similar approach. We note that we do not derive or provide a DGMF value for those filaments that are not associated with ATLASGAL clumps.

Comparing our DGMF calculation to that of other works, the calculation of dense gas mass and total mass of filaments in Ge & Wang (2022) both come from Herschel column density maps through the PPMAP approach (Marsh et al. 2017). They take circles guided by clumps in a given filament as the boundary of the dense gas and a combination of circles and rectangles guided by the filament as the boundary for the total mass calculation. The advantage of this calculation is that unification for data from different observations is not needed, and each pixel in a clump has a temperature measurement rather than a single temperature for the clump. However, the mass of unrelated structures that overlap with filaments in the projected sky may be incorrectly included in the mass calculation because the column density map is 2D. Ragan et al. (2014) and Abreu-Vicente et al. (2016) restricted their measurement via a mask created by ^{13}CO emission for both the dense gas mass and the total mass. They use the dust emission from the ATLASGAL 870 µm survey (Schuller et al. 2009) to calculate dense gas mass and ^{13}CO emission to calculate the total mass of filaments. Due to the limitations of the data available at that time, their temperature for the dense gas calculation had to be assumed, and the excitation temperature of ^{13}CO was assumed to be the same as that of ^{12}CO for the total mass calculation. Their dense gas mass and total mass are also not unified to the same dust opacity values.

To investigate whether the DGMF of filaments is related to their Galactic locations, we examined this quantity at different Galactocentric radii and Galactic heights in Fig. 5. As we can see, DGMFs in this work (red dots in the top two panels of Fig. 5) are not correlated with Galactocentric radius nor the Galactic height. An analysis of 163 ATLASGAL filaments (cyan stars in the top two panels of Fig. 5) provides similar results (Ge & Wang 2022). Here, we recalculated their DGMFs by changing the dense gas mass to be the mass of ATLASGAL clumps located within the filaments because the other three works we mention use this definition for the dense gas mass. Abreu-Vicente et al. (2016) also find that the DGMF is not correlated with Galactic height for their ten filaments in the fourth Galactic quadrant (green diamonds in Fig. 5b). Ragan et al. (2014) suggested that the DGMF decreases with increasing Galactocentric radius for their seven large-scale filaments, shown as yellow squares in Fig. 5a. These authors find that GMFs located closer to the Galactic mid-plane tend to have higher DGMF values than those significantly out of the plane (yellow squares in Fig. 5b). However, their filaments are selected as the densest and longest ones and they also indicate that the trends are weak and not statistically robust due to the small sample size. We note that comparing the absolute values of the DGMF across different works makes little sense unless they are unified carefully.

We also investigate how the DGMF may change between inter-arm filaments and filaments located within spiral arms. As shown in Fig. 5c, DGMFs in spiral arms or inter-arm regions have no clear differences (a KS-test gives a p-value of 0.5). The mean values of the DGMF for on-arm and off-arm filaments are 17.3 and 17.1%, respectively. Considering the tight relation between DGMF and star formation (e.g., Lada et al. 2012), we suggest that the star-forming potential in large-scale filaments has no distinct association with respect to their locations with spiral arms. This result is consistent with Ge & Wang (2022) but is contrary to the works of Ragan et al. (2014) and Abreu-Vicente et al. (2016). By analyzing 8 (Ragan et al. 2014) and 16 (Abreu-Vicente et al. 2016) filaments, such studies have found that the mean DGMF of spiral arm filaments is higher than that of the inter-arm filaments. Studies of giant molecular clouds have also reported that the DGMFs of molecular clouds exhibit no differences between the inter-arm and spiral-arm regions (Eden et al. 2013). Urquhart et al. (2021) found that there is no enhancement of dense gas in clouds with respect to their proximity to spiral arms. Other physical properties of molecular clouds such as effective radius, molecular gas mass, molecular gas mass surface density, and virial parameter have no significant differences between the spiral arms and inter-arm regions if the distance bias is avoided (Colombo et al. 2022). As for different arms, the mean DGMFs are 23.0% ± 5.6%, 9.4% ± 4.1%, and 7.6% ± 4.8% for filaments in the Scutum-Centaurus, Norma-Outer, and Sagittarius-Carina arms, respectively, where the uncertainties are the standard errors. Abreu-Vicente et al. (2016) also found that the mean DGMF of filaments in the Scutum-Centaurus arm is higher than those in the Sagittarius arm, but they lack a statistically significant sample. Of their nine filaments relating to spiral arms, only two are located within the Sagittarius arm and the other seven are within the Scutum-Centaurus arm. From the study of 1619 molecular clouds, Eden et al. (2021) found that DGMFs are similar for the Scutum–Centaurus, Sagittarius, and Perseus spiral arms. From a power-spectrum analysis, they also suggested that the largest variations in DGMF occur from cloud to cloud rather than on larger scales. That study is based upon CHIMPS molecular clouds from Rigby et al. (2016) that were extracted from ^{13}CO(3–2) after smoothing the original 15″ to a resolution of 27″ (thereby closely related to the tracer, ^{13}CO(2–1) and resolution of 28″ used in SEDIGISM). In addition, Rigby et al. (2019) found that most properties for their sample are indistinguishable between the Sagittarius and Scutum-Centaurus arms.

Spiral arms are important in gathering molecular gas (Wang et al. 2020a). However, the lack of any trends in DGMFs as a function of Galactic locations in the disk suggests that the conditions for star formation, which is directly related to DGMFs, is mostly unaffected by Galactocentric radius, Galactic height, and any association with spiral arms. Instead, the conditions for star formation are determined by factors at work on much smaller scales. This reinforces the conclusion from Wang et al. (2016) and is also consistent with the result of other studies asserting that the subsequent star formation processes after the cloud formation and HI to H_2 conversion depend more on the local environment (e.g., Urquhart et al. 2021; Colombo et al. 2022).

We go on consider whether DGMFs stand out in bones, investigating this issue by comparing DGMFs for bones and other filaments. As shown in Fig. 5d, for SEDIGISM filaments in this work (red boxes), the DGMFs of bones are significantly higher than for other filaments. We also classified GMFs (Ragan et al. 2014; Abreu-Vicente et al. 2016) into bones and other filaments according to criteria in Sect. 4.1.1. The GMFs from Ragan et al. (2014) are all classified as other non-bone filaments due to their departure from spiral arms or verticality to the Galactic plane. Four GMFs from Abreu-Vicente et al. (2016) pass the bone criteria and are classified as bones. DGMFs of GMFs for bones and other filaments are plotted as blue boxes in Fig. 5d. For bones, DGMFs are also obviously larger than other

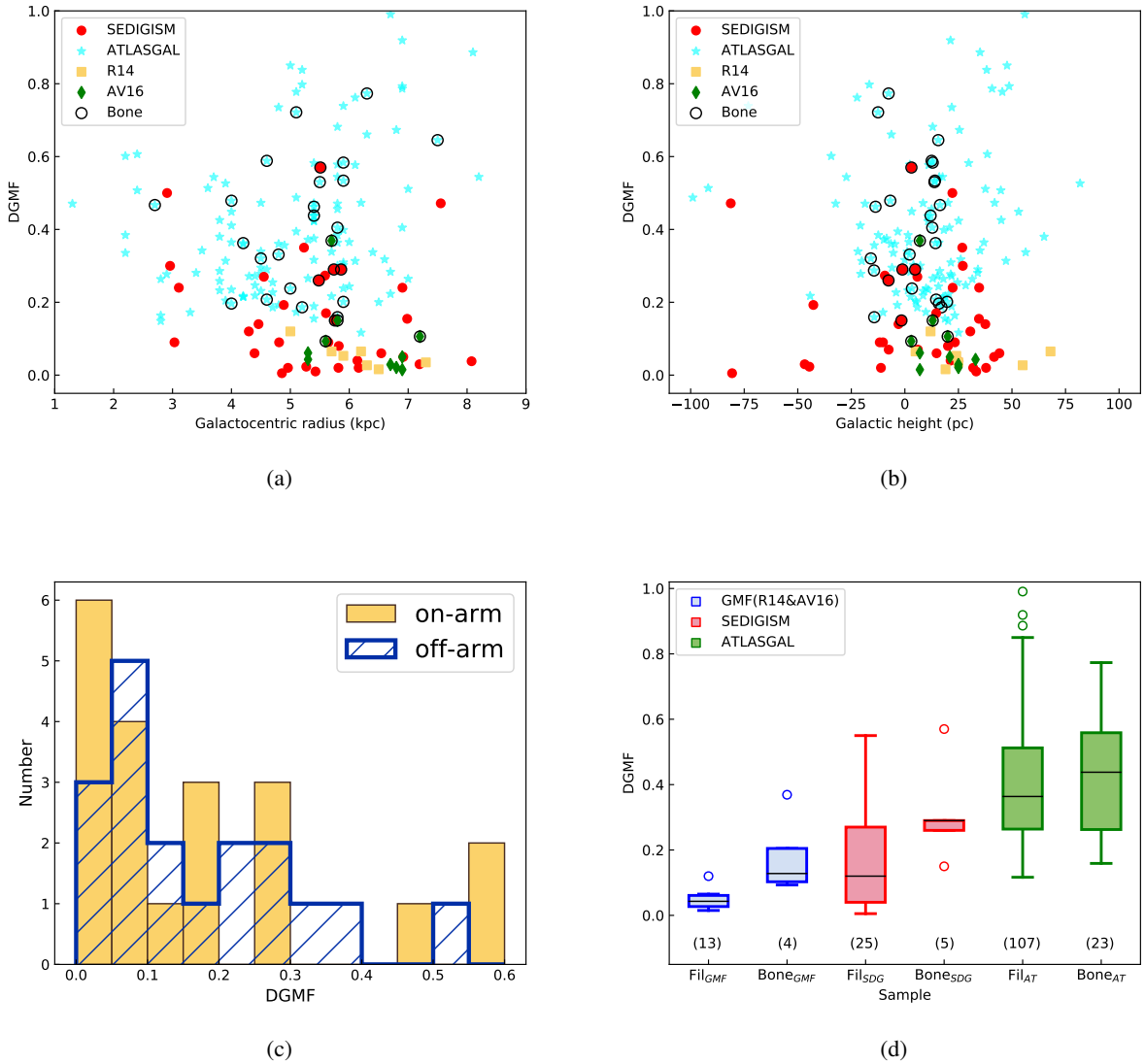

Fig. 5. DGMFs of large-scale filaments. (a) DGMFs of large-scale filaments as a function of Galactocentric radius. Red-filled circles show DGMFs for filaments in this work. Cyan stars represent those from ATLASGAL filaments (Ge & Wang 2022). Yellow squares denote filaments from Ragan et al. (2014) and green diamonds are from Abreu-Vicente et al. (2016). If a filament also satisfies the bone criteria, a black circle is added to the polygon; (b) DGMF versus Galactic height. Symbols follow the convention of panel a; (c) the distribution of DGMFs for on-arm or off-arm filaments. Yellow bars denote filaments in spiral arms and blue hatch marks inter-arm filaments; (d) differences in DGMF between bones and other filaments for three samples. Red boxes are SEDIGISM filaments from this work. Blue boxes represent GMFs from Ragan et al. (2014); Abreu-Vicente et al. (2016). Green boxes mark ATLASGAL filaments. The right boxes for each color are bones and the left ones are other filaments. A box extends from the first quartile to the third quartile of the data, with a line at the median. The whiskers extending from the boxes enclose all of the data except outliers, which are denoted as dots. Numbers above the bottom border are the numbers of bones or other filaments.

filaments, which is the same as the result for filaments in this work. For ATLASGAL filaments (green boxes), this difference is not so evident. Only the median DGMF is a bit higher for bones than for other filaments. To summarize, we collect DGMFs of 4 bones and 13 other filaments from Ragan et al. (2014) and Abreu-Vicente et al. (2016), and 23 bones and 107 other filaments from Ge & Wang (2022), as well as 5 bones and 25 other filaments from SEDIGISM filaments in this work. If we exclude redundant filaments that are identified several times by different works, the total sample size for DGMFs is 168. It seems that bones (i.e., filaments located at the very center of spiral arms) potentially stand out in DGMFs when compared to other filaments, thereby promoting star formation activity. On the one hand, the number of known bones is still small. On the other hand, the dust continuum is may not always serve as a good tracer of dense gas due to optical depth effects. Therefore, in the future, we will collect more bones to investigate this issue. In addition, we will employ an optically thin dense gas tracer (such as N_2H^+) to recalculate the dense gas content.

5. Summary

We built a catalog of 88 large-scale ^{13}CO filaments in the inner Galactic plane ($-60° < l < 18°$, $|b| < 0.^{\circ}5$). The catalog is composed of 55 large-scale filaments identified through SEDIGISM leaves using MST and 33 large elongated filaments selected from the SEDIGISM cloud catalog. Our main results are summarized as follows.

1. Of the 88 filaments considered in our study, 66 are not included in the former large-scale filament catalogs. The

^{13}CO emission can trace relatively diffuse structures with lower density than continuum surveys such as BGPS and ATLASGAL.
2. We compared the physical properties of our filaments to MST filaments identified through BGPS and ATLASGAL sources. The ^{13}CO filaments are on average longer than the other two (based on the dust continuum). The column density and line mass of our filaments are lower than the other two.
3. We investigated the association of our filaments with the Galactic spiral arms to determine whether they satisfy the criteria to be considered as Galactic bones. We find half of the filaments are associated with spiral arms in PV space. We found eight bone candidates for the Milky Way.
4. From the study of Galactic spur and large-scale filaments, we found that three filaments satisfy the criteria for bones associated with the Local spur in PPV space. Thus, we suggest that they may be bone candidates of the Local spur.
5. By compiling 168 large-scale filaments with unified DGMFs across the Galaxy, which is an order of magnitude more than previously investigated, we find that DGMFs of large-scale filaments are not correlated with Galactocentric radius or Galactic height. The DGMFs of filaments in spiral arms or inter-arm regions have no distinct differences. However, a further comparison between bones and other filaments indicates that bones have higher DGMFs than other filaments.

The census of large-scale filaments is helpful for our understanding of the Galactic structures. We could also study star formation on the Galactic scale by inspecting DGMFs of large-scale filaments.

Acknowledgements. We thank Ligang Hou, Siju Zhang, Nannan Yue, Fengwei Xu, Chao Wang, Wenyu Jiao, and Juan Diego Soler for the helpful discussion. We thank an anonymous referee for constructive comments, which have significantly improved the manuscript. We acknowledge support from the National Science Foundation of China (12033005, 11973013), the China Manned Space Project (CMS-CSST-2021-A09), the National Key Research and Development Program of China (2022YFA1603102, 2019YFA0405100), and the High-Performance Computing Platform of Peking University. DC acknowledges support by the German Deutsche Forschungsgemeinschaft, DFG project number SFB956A. ADC acknowledges the support of the Royal Society University Research Fellowship (URF/R1/191609). HB acknowledges support from the Deutsche Forschungsgemeinschaft in the Collaborative Research Center (SFB 881) "The Milky Way System" (subproject B1). L.B. gratefully acknowledges support by the ANID BASAL projects ACE210002 and FB210003. C.L.D. acknowledges funding from the European Research Council for the Horizon 2020 ERC consolidator grant project ICYBOB, grant number 818940. This publication is based on data acquired with the Atacama Pathfinder Experiment (APEX) under programs 092.F-9315 and 193.C-0584. APEX is a collaboration among the Max-Planck-Institut fur Radioastronomie, the European Southern Observatory, and the Onsala Space Observatory. The processed data products are available from the SEDIGISM survey database located at `https://sedigism.mpifr-bonn.mpg.de/index.html`, which was constructed by James Urquhart and hosted by the Max Planck Institute for Radio Astronomy.

References

Abreu-Vicente, J., Ragan, S., Kainulainen, J., et al. 2016, A&A, 590, A131
Adami, C., & Mazure, A. 1999, A&AS, 134, 393
Alpaslan, M., Robotham, A. S. G., Driver, S., et al. 2014, MNRAS, 438, 177
Andre, P., Men'shchikov, A., Bontemps, S., et al. 2010, A&A, 518, L102
Arzoumanian, D., André, P., Didelon, P., et al. 2011, A&A, 529, L6
Arzoumanian, D., André, P., Könyves, V., et al. 2019, A&A, 621, A42
Barrow, J. D., Bhavsar, S. P., & Sonoda, D. H. 1985, MNRAS, 216, 17
Battersby, C., Ginsburg, A., Bally, J., et al. 2014, ApJ, 787, 113
Battisti, A. J., & Heyer, M. H. 2014, ApJ, 780, 172
Carey, S. J., Noriega-Crespo, A., Mizuno, D. R., et al. 2009, PASP, 121, 76
Cartwright, A., & Whitworth, A. P. 2004, MNRAS, 348, 589
Chen, X., Sun, L., Feng, J., et al. 2023, ApJ, 165,1
Clarke, S. D., Sánchez-Monge, A., Williams, G. M., et al. 2023, MNRAS, 519, 3098
Colberg, J. M. 2007, MNRAS, 375, 337
Colombo, D., Rosolowsky, E., Ginsburg, A., Duarte-Cabral, A., & Hughes, A. 2015, MNRAS, 454, 2067
Colombo, D., Rosolowsky, E., Duarte-Cabral, A., et al. 2019, MNRAS, 483, 4291
Colombo, D., König, C., Urquhart, J. S., et al. 2021, A&A, 655, L2
Colombo, D., Duarte-Cabral, A., Pettitt, A. R., et al. 2022, A&A, 658, A54
Cordes, J. M. 2004, ASP Conf. Ser., 317, 211
Cox, N. L. J., Arzoumanian, D., André, P., et al. 2016, A&A, 590, A110
Dib, S., & Henning, T. 2019, A&A, 629, A135
Dobbs, C. L., & Bonnell, I. A. 2006, MNRAS, 367, 873
Doroshkevich, A., Tucker, D. L., Allam, S., & Way, M. J. 2004, A&A, 418, 7
Du, X., Xu, Y., Yang, J., & Sun, Y. 2017, ApJS, 229, 24
Duarte-Cabral, A., & Dobbs, C. L. 2016, MNRAS, 458, 3667
Duarte-Cabral, A., Colombo, D., Urquhart, J. S., et al. 2021, MNRAS, 500, 3027
Eden, D. J., Moore, T. J. T., Morgan, L. K., Thompson, M. A., & Urquhart, J. S. 2013, MNRAS, 431, 1587
Eden, D. J., Moore, T. J. T., Plume, R., et al. 2021, MNRAS, 500, 191
Elia, D., Molinari, S., Fukui, Y., et al. 2013, ApJ, 772, 45
Ge, Y., & Wang, K. 2022, ApJS, 259, 36
Goodman, A. A., Alves, J., Beaumont, C. N., et al. 2014, ApJ, 797, 53
Guo, W., Chen, X., Feng, J., et al. 2022, ApJ, 938, 44
Gutermuth, R. A., Megeath, S. T., Myers, P. C., et al. 2009, ApJS, 184, 18
Hou, L. G. 2021, Front. Astron. Space Sci., 8, 103
Jackson, J. M., Finn, S. C., Chambers, E. T., Rathborne, J. M., & Simon, R. 2010, ApJ, 719, L185
Jaffa, S. E., Whitworth, A. P., Clarke, S. D., & Howard, A. D. P. 2018, MNRAS, 477, 1940
Johnstone, D., & Bally, J. 1999, ApJ, 510, L49
Joung, M. K. R., & Mac Low, M.-M. 2006, ApJ, 653, 1266
Kim, W.-T., & Ostriker, E. C. 2006, ApJ, 646, 213
Kim, W.-T., Kim, C.-G., & Ostriker, E. C. 2020, ApJ, 898, 35
Koch, E. W., & Rosolowsky, E. W. 2015, MNRAS, 452, 3435
Kohno, M., Nishimura, A., Fujita, S., et al. 2022, PASJ, 74, 24
Lada, C. J., Forbrich, J., Lombardi, M., & Alves, J. F. 2012, ApJ, 745, 190
Li, G.-X., Wyrowski, F., Menten, K., & Belloche, A. 2013, A&A, 559, A34
Li, G. X., Urquhart, J. S., Leurini, S., et al. 2016, A&A, 591, A5
Li, G.-X., Zhou, J.-X., & Chen, B.-Q. 2022, MNRAS, 516, L35
Lin, L.-H., Wang, H.-C., Su, Y., Li, C., & Yang, J. 2020, Res. Astron. Astrophys., 20, 143
Liu, H. B., Quintana-Lacaci, G., Wang, K., et al. 2012, ApJ, 745, 61
Liu, T., Zhang, Q., Kim, K.-T., et al. 2016, ApJ, 824, 31
Liu, H.-L., Stutz, A., & Yuan, J.-H. 2018, MNRAS, 478, 2119
Mandowara, Y., Sormani, M. C., Sobacchi, E., & Klessen, R. S. 2022, MNRAS, 513, 5052
Marsh, K. A., Whitworth, A. P., Lomax, O., et al. 2017, MNRAS, 471, 2730
Mattern, M., Kauffmann, J., Csengeri, T., et al. 2018, A&A, 619, A166
Molinari, S., Swinyard, B., Bally, J., et al. 2010, PASP, 122, 314
Naidoo, K., Whiteway, L., Massara, E., et al. 2020, MNRAS, 491, 1709
Neralwar, K. R., Colombo, D., Duarte-Cabral, A., et al. 2022, A&A, 663, A56
Ostriker, J. 1964, ApJ, 140, 1056
Palmeirim, P., André, P., Kirk, J., et al. 2013, A&A, 550, A38
Park, D., & Lee, J. 2009, MNRAS, 397, 2163
Pearson, K. 1901, Philos. Mag., 2, 559
Peretto, N., Fuller, G. A., Duarte-Cabral, A., et al. 2013, A&A, 555, A112
Peretto, N., Fuller, G. A., Andre, P., et al. 2014, A&A, 561, A83
Pereyra, L. A., Sgró, M. A., Merchán, M. E., Stasyszyn, F. A., & Paz, D. J. 2020, MNRAS, 499, 4876
Pettitt, A. R., Dobbs, C. L., Baba, J., et al. 2020, MNRAS, 498, 1159
Pilbratt, G. L., Riedinger, J. R., Passvogel, T., et al. 2010, A&A, 518, L1
Pillai, T., Kauffmann, J., Zhang, Q., et al. 2019, A&A, 622, A54
Ragan, S. E., Henning, T., Tackenberg, J., et al. 2014, A&A, 568, A73
Reid, M. J., Menten, K. M., Brunthaler, A., et al. 2019, ApJ, 885, 131
Rickard, J. J., & Cronyn, W. M. 1979, ApJ, 228, 755
Rigby, A. J., Moore, T. J. T., Plume, R., et al. 2016, MNRAS, 456, 2885
Rigby, A. J., Moore, T. J. T., Eden, D. J., et al. 2019, A&A, 632, A58
Rosolowsky, E. W., Pineda, J. E., Kauffmann, J., & Goodman, A. A. 2008, ApJ, 679, 1338
Sanhueza, P., Contreras, Y., Wu, B., et al. 2019, ApJ, 886, 102
Schisano, E., Rygl, K. L. J., Molinari, S., et al. 2014, ApJ, 791, 27
Schisano, E., Molinari, S., Elia, D., et al. 2020, MNRAS, 492, 5420
Schmalzl, M., Kainulainen, J., Quanz, S. P., et al. 2010, ApJ, 725, 1327
Schmeja, S., & Klessen, R. S. 2006, A&A, 449, 151
Schneider, S., & Elmegreen, B. G. 1979, ApJS, 41, 87

Schuller, F., Menten, K. M., Contreras, Y., et al. 2009, A&A, 504, 415
Schuller, F., Csengeri, T., Urquhart, J. S., et al. 2017, A&A, 601, A124
Schuller, F., Urquhart, J. S., Csengeri, T., et al. 2021, MNRAS, 500, 3064
Smith, R. J., Glover, S. C. O., Clark, P. C., Klessen, R. S., & Springel, V. 2014, MNRAS, 441, 1628
Smith, R. J., Treß, R. G., Sormani, M. C., et al. 2020, MNRAS, 492, 1594
Sofue, Y. 1976, A&A, 48, 1
Sokolov, V., Wang, K., Pineda, J. E., et al. 2017, A&A, 606, A133
Sokolov, V., Wang, K., Pineda, J. E., et al. 2018, A&A, 611, L3
Sokolov, V., Wang, K., Pineda, J. E., et al. 2019, ApJ, 872, 30
Soler, J. D., Beuther, H., Syed, J., et al. 2021, A&A, 651, L4
Soler, J. D., Miville-Deschênes, M. A., Molinari, S., et al. 2022, A&A, 662, A96
Tang, Y.-W., Koch, P. M., Peretto, N., et al. 2019, ApJ, 878, 10
Taylor, J. H., & Cordes, J. M. 1993, ApJ, 411, 674
Torii, K., Fujita, S., Nishimura, A., et al. 2019, PASJ, 71, 1
Urquhart, J. S., Figura, C., Cross, J. R., et al. 2021, MNRAS, 500, 3050
Veena, V. S., Schilke, P., Sánchez-Monge, A., et al. 2021, ApJ, 921, L42
Wada, K., & Koda, J. 2004, MNRAS, 349, 270
Wang, K., & Ge, Y. 2021, Astrophysics Source Code Library [record ascl:2102.002]
Wang, K., Zhang, Q. Z., Testi, L., et al. 2014, MNRAS, 439, 3275
Wang, K., Testi, L., Ginsburg, A., et al. 2015, MNRAS, 450, 4043
Wang, K., Testi, L., Burkert, A., et al. 2016, ApJS, 226, 9
Wang, Y., Beuther, H., Rugel, M. R., et al. 2020a, A&A, 634, A139
Wang, Y., Beuther, H., Schneider, N., et al. 2020b, A&A, 641, A53
Watkins, E. J., Peretto, N., Marsh, K., & Fuller, G. A. 2019, A&A, 628, A21
Wu, B., Tan, J. C., Christie, D., et al. 2017, ApJ, 841, 88
Xu, Y., Reid, M., Dame, T., et al. 2016, Sci. Astron., 2, e1600878
Xu, F.-W., Wang, K., Liu, T., et al. 2023, MNRAS, 520, 3259
Yuan, J., Li, J.-Z., Wu, Y., et al. 2018, ApJ, 852, 12
Zhang, M., Kainulainen, J., Mattern, M., Fang, M., & Henning, T. 2019, A&A, 622, A52
Zhang, S., Wang, K., Liu, T., et al. 2023, MNRAS, 520, 322
Zucker, C., Battersby, C., & Goodman, A. 2015, ApJ, 815, 23
Zucker, C., Battersby, C., & Goodman, A. 2018, ApJ, 864, 153
Zucker, C., Smith, R., & Goodman, A. 2019, ApJ, 887, 186

Appendix A: A summary of physical properties of large-scale filaments

Table A.1: Physical properties of large-scale filaments

(1) ID	(2) Origin	(3) l_{wt} (°)	(4) b_{wt} (°)	(5) v_{wt} (km s^{-1})	(6) d (kpc)	(7) N	(8) $L_{\rm sum}$ (pc)	(9) L_{end} (pc)	(10) Mass ($10^3 M_\odot$)	(11) M_{line} ($M_\odot$ pc^{-1})	(12) N_{H_2} (10^{22} cm^{-2})	(13) f_A	(14) f_L	(15) R_{gc} (kpc)	(16) z (pc)	(17) $\lvert\theta\rvert$ (°)	(18) DGMF	(19) Morph. class	(20) Arm	(21) Ref.
M1	MST	300.85±0.01	0.27±0.03	-36.1±0.3	4.3±0.1	6	21.3	14.6	1.5	68.5	0.2	4.10	2.50	7.2	42.1±2.0	77.5±3.0	-	C,X		
M2	MST	302.79±0.03	0.15±0.02	-34.8±0.4	5.7±0.5	6	35.4	21.0	8.8	247.7	0.5	2.90	2.16	7.1	35.6±2.0	28.2±2.8	-	C		
M3	MST	305.07±0.02	0.14±0.04	-38.2±0.6	6.1±0.5	7	55.6	35.0	6.3	113.4	0.4	8.14	3.91	7.0	34.6±3.9	70.5±1.5	0.15	C,X		GMF307 (1); F163 (5)
M4	MST	305.50±0.02	0.09±0.03	-36.2±0.3	6.6±0.5	6	35.0	24.5	8.8	250.3	0.4	4.32	1.84	7.0	29.7±3.3	75.1±3.5	-	C		GMF307 (1)
M5	MST	320.64±0.01	0.09±0.02	-5.2±0.7	12.6±0.1	6	56.1	35.9	17.0	303.2	0.4	7.13	3.70	8.1	25.1±5.0	86.0±2.8	0.04	L		
M6	MST	324.19±0.02	-0.08±0.01	-56.5±0.2	10.1±1.0	10	70.7	42.9	8.7	123.8	0.2	4.78	2.05	5.9	-5.2±2.4	23.1±2.3	-	X	Scu-Cen, Bone	
M7	MST	324.28±0.04	-0.39±0.01	-32.1±0.2	11.5±1.6	7	75.5	68.9	19.4	257.1	0.4	8.75	6.10	6.8	-73.0±1.8	6.9±1.3	-	S		GMF324 (1)
M8	MST	326.86±0.03	-0.10±0.02	-62.6±0.3	10.2±1.0	6	63.8	48.1	20.4	318.8	0.5	5.87	3.91	5.6	-9.4±4.0	31.8±1.8	0.27	H		F142 (5)
M9	MST	327.03±0.02	-0.17±0.02	-56.5±0.4	10.6±0.7	9	69.4	39.9	11.6	167.1	0.3	3.48	2.64	5.8	-24.2±2.9	30.3±2.0	-	H	Scu-Cen	F141 (5)
M10	MST	334.07±0.04	-0.40±0.02	-47.2±0.2	11.9±0.8	10	128.9	75.7	33.6	260.5	0.3	4.19	2.89	5.7	-80.5±3.6	16.1±1.1	-	S,X	Nor-Out	
M11	MST	334.95±0.03	-0.34±0.02	-90.0±0.4	5.3±0.9	7	36.1	21.2	4.3	120.5	0.2	3.87	1.77	4.2	-16.5±1.6	21.1±3.3	-	X	Nor-Out	Fil9 (2)
M12	MST	336.47±0.01	-0.05±0.02	-127.1±0.6	7.6±0.1	7	44.8	25.1	3.0	66.8	0.1	7.70	3.96	3.3	3.5±3.0	86.4±2.3	-	L,X		
M13	MST	337.25±0.02	-0.21±0.02	-114.6±0.4	8.4±0.2	10	62.4	35.7	7.2	115.2	0.2	3.88	2.09	3.3	-22.1±3.1	55.1±2.2	-	X		
M14	MST	337.12±0.01	0.11±0.03	-75.6±0.3	10.7±0.1	6	55.9	47.2	7.1	126.6	0.2	10.05	4.80	4.4	24.6±6.1	72.6±1.9	-	S		
M15	MST	337.22±0.03	-0.04±0.01	-52.3±0.3	11.9±1.6	6	54.9	42.7	9.9	180.7	0.3	6.37	2.98	5.3	-6.1±3.0	20.3±2.4	-	C		
M16	MST	336.61±0.02	0.44±0.02	-33.0±0.2	12.9±1.6	6	67.5	40.6	11.7	172.9	0.2	3.96	1.75	6.2	98.0±5.1	55.8±4.4	-	S		
M17	MST	338.26±0.03	-0.06±0.02	-44.0±0.6	12.3±1.4	6	72.3	51.1	20.7	286.4	0.3	5.14	2.76	5.5	-12.2±4.1	34.6±2.6	-	X	Scu-Cen	
M18	MST	338.37±0.03	-0.16±0.01	-90.5±0.5	10.1±0.6	7	48.0	40.3	14.4	300.6	0.4	8.43	5.23	3.9	-23.3±2.1	21.1±1.8	-	L,H		
M19	MST	336.22±0.03	0.34±0.01	-70.3±0.5	10.9±1.3	6	49.8	41.3	4.3	86.6	0.2	20.82	5.46	4.7	67.5±1.9	15.7±2.1	-	L,X		
M20	MST	339.43±0.04	-0.16±0.02	-119.0±0.5	8.4±0.2	6	59.6	38.5	9.3	155.4	0.2	4.44	2.74	3.0	-15.2±2.3	12.7±2.1	-	X		
M21	MST	343.92±0.01	0.32±0.02	-67.5±0.5	5.0±1.1	7	25.6	14.3	0.8	32.6	0.1	4.81	1.83	3.8	43.1±1.6	85.7±3.8	-	X	Nor-Out	
M22	MST	344.67±0.02	-0.43±0.02	-21.9±0.8	13.9±1.8	6	58.8	37.2	7.1	120.7	0.2	6.08	2.01	6.3	-108.9±3.8	44.5±4.7	-	X	Nor-Out	
M23	MST	325.73±0.02	0.42±0.03	-41.1±0.2	2.5±1.7	6	13.0	8.6	1.0	74.5	0.2	4.15	2.11	6.4	39.5±1.1	57.3±3.1	-	S,X		
M24	MST	349.91±0.02	-0.25±0.01	-24.1±0.4	3.3±1.7	9	24.4	14.0	1.8	72.4	0.1	4.20	1.85	5.3	3.6±0.8	16.5±2.7	-	X	Perseus, Bone	
M25	MST	352.36±0.01	-0.20±0.02	-84.9±0.2	8.2±0.2	8	42.7	22.1	4.8	112.6	0.2	2.63	1.95	1.3	-22.1±2.9	75.9±3.5	-	C		
M26	MST	353.02±0.03	-0.07±0.01	-17.6±0.2	13.4±1.4	12	125.0	72.4	26.4	211.3	0.3	4.00	2.92	5.3	-21.5±2.2	2.3±1.2	-	S,X	Scu-Cen	
M27	MST	353.20±0.02	-0.34±0.01	-17.6±0.3	13.4±0.1	9	68.3	38.9	11.2	164.4	0.2	3.95	2.07	5.2	-84.3±2.4	15.1±3.3	-	C	Scu-Cen	
M28	MST	353.75±0.01	0.06±0.03	1.9±0.5	18.1±0.2	6	111.2	63.6	18.4	165.7	0.1	6.11	2.82	9.8	5.4±8.6	71.7±2.6	-	L,X	Scu-Cen	
M29	MST	356.87±0.02	0.06±0.03	4.9±0.3	21.0±0.1	8	173.7	77.2	40.4	232.7	0.2	2.04	1.82	12.7	2.8±10.3	76.8±2.7	-	C,X	Scu-Cen	GMF358 (1)
M30	MST	358.28±0.04	-0.69±0.01	-21.4±0.3	9.7±0.5	6	63.3	42.3	3.4	54.1	0.1	4.55	2.70	1.4	-113.2±2.4	5.4±2.0	-	S		
M31	MST	358.87±0.01	-0.26±0.03	-3.2±0.6	15.9±0.7	7	106.4	56.2	21.1	197.9	0.2	3.51	2.86	7.6	-81.3±7.6	77.5±2.4	0.47	X	Scu-Cen	
M32	MST	358.84±0.02	-0.06±0.01	-193.2±0.4	8.4±0.1	6	26.2	21.0	1.7	64.0	0.1	5.44	4.88	0.2	-2.4±1.0	12.3±3.0	-	S		
M33	MST	0.80±0.03	0.29±0.01	170.0±0.5	8.4±0.1	7	50.1	30.0	2.5	49.9	0.1	10.89	4.82	0.2	49.7±0.8	0.6±1.4	-	C,X		
M34	MST	0.95±0.01	0.34±0.01	160.7±0.8	8.4±0.1	6	31.5	14.1	1.7	54.2	0.1	6.05	4.23	0.2	56.1±2.2	61.9±4.1	-	X		
M35	MST	3.12±0.02	0.14±0.01	134.7±0.4	8.3±0.1	6	37.7	23.2	4.2	111.3	0.2	4.14	1.65	0.5	27.3±2.1	28.7±5.6	-	X		
M36	MST	6.12±0.02	-0.18±0.02	13.6±1.0	13.2±1.2	14	203.2	74.0	49.5	243.8	0.3	5.84	3.07	5.3	-44.6±3.5	31.8±1.2	0.02	X	Scu-Cen	F2 (5)
M37	MST	5.96±0.03	-0.33±0.01	7.3±0.2	15.0±1.9	11	140.7	80.7	85.7	608.7	0.9	5.28	2.02	6.7	-94.5±3.8	8.1±1.7	-	C	Perseus	
M38	MST	6.69±0.02	-0.08±0.03	19.1±0.8	12.6±1.7	7	97.3	51.4	22.4	230.0	0.3	3.67	2.37	4.8	-20.4±6.1	63.3±2.3	-	X	Scu-Cen	
M39	MST	6.66±0.02	-0.14±0.03	5.8±0.4	15.4±1.9	7	95.8	70.5	46.5	485.3	0.6	4.13	2.83	7.2	-46.8±7.9	63.9±2.0	0.03	C	Sag-Car	
M40	MST	7.01±0.03	0.22±0.02	15.4±0.4	13.8±0.1	6	100.3	62.8	19.1	190.4	0.2	3.79	1.94	5.6	49.1±4.5	18.4±2.9	-	X	Scu-Cen	
M41	MST	7.59±0.02	-0.29±0.01	149.4±0.4	8.3±0.1	6	33.0	18.5	1.2	35.2	0.1	3.12	2.22	1.1	-34.5±1.6	26.3±4.7	-	S		
M42	MST	8.13±0.02	-0.32±0.03	136.6±0.6	8.3±0.1	7	62.2	40.8	3.6	57.7	0.1	3.28	2.06	1.2	-39.4±5.0	64.2±2.1	-	S		
M43	MST	8.63±0.03	-0.10±0.02	32.4±0.4	12.3±1.0	7	74.7	49.1	55.3	740.6	0.6	6.69	2.55	4.2	-22.1±3.7	27.4±2.3	-	C	Sag-Car	
M44	MST	10.50±0.03	-0.33±0.01	13.2±0.7	14.5±2.4	6	89.9	56.1	12.2	135.9	0.2	4.15	2.74	6.5	-88.2±2.8	3.0±2.1	-	S	Perseus	F5 (4)
M45	MST	10.31±0.01	0.37±0.03	31.1±0.3	12.7±1.5	7	69.7	54.1	22.9	328.4	0.3	8.22	3.87	4.7	80.7±6.6	81.3±2.0	-	L,H	Sag-Car	
M46	MST	13.71±0.02	-0.37±0.02	40.0±0.4	12.4±1.2	13	176.0	74.2	104.2	592.2	0.5	2.76	1.89	4.9	-80.7±3.3	20.4±1.7	0.01	X	Sag-Car	

Continued on next page

Table A.1: Physical properties of large-scale filaments

(1) ID	(2) Origin	(3) l_{wt} (°)	(4) b_{wt} (°)	(5) v_{wt} (km s^{-1})	(6) d (kpc)	(7) N	(8) $L_{\rm sum}$ (pc)	(9) L_{end} (pc)	(10) Mass ($10^3 M_\odot$)	(11) M_{line} ($M_\odot$ pc^{-1})	(12) N_{H_2} (10^{22} cm^{-2})	(13) f_A	(14) f_L	(15) R_{gc} (kpc)	(16) z (pc)	(17) $\|\theta\|$ (°)	(18) DGMF	(19) Morph. class	(20) Arm	(21) Ref.
M47	MST	14.84±0.03	-0.38±0.02	26.0±0.3	2.8±2.0	7	17.9	12.3	0.3	17.3	0.0	6.48	3.38	5.8	1.2±0.8	24.2±1.8	-	S		
M48	MST	14.94±0.01	-0.32±0.03	30.9±0.4	13.2±0.1	7	80.4	55.5	21.8	271.1	0.3	6.85	4.52	5.6	-75.4±6.2	64.3±1.9	-	S		
M49	MST	14.59±0.03	-0.45±0.01	18.4±0.6	14.1±0.1	11	112.7	66.6	28.9	256.6	0.3	4.35	4.15	6.4	-114.6±1.8	4.8±1.3	-	S	Perseus	
M50	MST	14.58±0.01	0.12±0.02	35.0±0.1	12.9±0.1	9	91.9	49.0	19.4	211.0	0.2	4.22	1.91	5.2	25.6±4.5	60.0±3.0	-	C,X	Scu-Cen	
M51	MST	14.69±0.02	0.15±0.01	39.4±0.3	12.5±1.6	8	75.9	48.2	12.9	170.4	0.3	5.72	2.88	5.0	32.0±2.5	19.2±2.3	-	S,X	Scu-Cen	
M52	MST	15.09±0.02	0.18±0.01	28.4±0.6	13.3±1.4	7	84.9	39.0	15.4	181.3	0.2	3.70	2.48	5.7	38.5±3.0	29.3±3.2	-	X		
M53	MST	16.66±0.02	-0.20±0.03	46.7±0.5	12.2±1.0	8	89.6	66.1	19.0	212.1	0.2	9.04	4.64	4.9	-42.7±6.8	61.9±1.3	0.19	S	Sag-Car	
M54	MST	16.68±0.01	-0.13±0.03	36.9±0.7	12.7±1.9	6	60.1	40.0	14.6	243.0	0.4	5.50	2.54	5.4	-30.5±6.2	80.2±2.9	-	C		
M55	MST	16.79±0.03	0.37±0.03	23.7±0.4	13.7±2.0	8	117.2	68.6	92.0	785.1	0.9	3.98	1.84	6.2	85.3±7.0	52.8±2.1	-	C,X	Perseus	
S56	320	305.70	0.33	-39.2±3.2	3.5±1.0	7	27.9	12.3	6.3	227.4	0.6	3.87	-	6.9	41.7	87.9	0.05	S	Scu-Cen	GMF307 (1)
S57	852	312.62	0.03	-63.8±1.4	5.7±1.4	11	64.3	31.6	48.5	755.0	0.9	6.13	-	6.1	21.3	8.0	0.04	S,X		
S58	1421	317.64	-0.13	-44.4±3.0	2.8±0.6	6	15.0	6.9	3.6	242.1	0.8	4.31	-	6.5	14.8	10.3	0.06	S		GMF319 (1)
S59	1772	320.25	0.36	-32.5±1.0	2.0±0.5	5	22.9	6.9	6.3	276.3	0.6	3.64	-	6.9	34.7	68.7	0.24	L,H		
S60	1879	323.49	0.07	-66.3±1.3	4.0±0.5	5	34.4	13.6	26.4	768.5	0.8	4.10	-	5.6	23.3	34.7	0.09	C		
S61	2590	328.05	0.37	-44.9±1.0	2.8±0.5	6	33.7	13.5	8.8	260.3	0.4	5.27	-	6.2	37.9	31.1	0.02	S		
S62	2884	330.53	0.23	-61.6±2.0	3.7±0.4	7	41.0	17.5	13.9	338.9	0.5	3.63	-	5.4	33.3	14.3	0.01	C	Nor-Out	
S63	2942	330.32	0.29	-96.1±1.4	5.8±0.7	8	57.2	20.8	33.5	586.2	0.5	3.84	-	4.4	44.1	27.8	0.06	S	Nor-Out	
S64	2947	331.69	0.01	-48.7±2.7	3.1±0.5	16	41.9	18.3	28.1	670.3	0.9	5.49	-	5.8	20.1	19.2	0.08	C	Scu-Cen	F130 (5)
S65	3108	331.52	-0.11	-87.6±2.8	5.1±0.5	17	60.6	21.8	213.8	3527.1	1.7	3.55	-	4.6	5.8	17.2	0.27	S		F130 (5)
S66	3129	331.61	-0.28	-47.9±1.0	3.0±0.5	6	16.1	8.4	8.1	501.2	1.0	4.58	-	5.9	4.8	18.7	0.29	C	Scu-Cen, Bone	
S67	3233	332.10	-0.43	-57.0±2.8	3.5±0.4	10	21.6	8.5	24.4	1129.4	1.9	3.85	-	5.5	-7.6	24.7	0.26	C,H	Nor-Out, Bone	F129 (5)
S68	3423	334.22	0.17	-88.8±3.9	5.2±0.5	5	67.9	25.0	33.7	496.0	0.4	3.92	-	4.3	30.6	30.1	0.12	S	Nor-Out	
S69	4022	336.80	0.27	-75.6±2.1	4.7±0.4	6	19.1	8.4	6.2	326.6	0.7	4.06	-	4.5	37.6	10.1	0.14	S		
S70	4449	336.70	0.25	-40.9±1.3	2.9±0.5	7	23.1	12.3	4.1	175.5	0.4	4.05	-	5.8	31.9	46.7	0.02	C,X	Nor-Out	
S71	4698	337.68	-0.40	-41.0±1.3	2.9±0.5	33	64.9	25.2	72.4	1115.9	0.8	3.77	-	5.7	-1.2	0.1	0.29	S,H	Scu-Cen, Bone	Nessie (3); F113 (5)
S72	4930	339.19	-0.42	-38.1±1.4	2.9±0.5	8	31.6	13.3	14.4	454.9	0.7	4.19	-	5.8	-1.6	1.3	0.15	S	Scu-Cen, Bone	Nessie (3)
S73	5079	339.57	0.09	-110.6±1.5	6.7±0.6	5	59.5	21.5	52.0	873.5	0.7	4.88	-	3.1	22.3	6.3	0.24	L		
S74	5539	342.58	0.15	-41.6±1.2	3.4±0.5	6	25.7	12.7	23.8	927.0	0.9	4.72	-	5.2	26.8	11.3	0.35	S		GMF343 (1); F99 (5)
S75	5774	344.96	-0.24	-85.9±1.0	5.9±0.4	6	47.2	16.9	37.3	789.3	0.6	3.81	-	3.0	-11.7	10.4	0.09	C		
S76	6191	349.21	0.14	-64.0±2.7	5.7±0.4	7	53.6	21.5	42.0	783.6	0.6	4.95	-	3.0	27.1	3.6	0.30	S		F83 (5)
S77	6300	349.86	0.09	-61.4±1.7	5.7±0.4	5	35.2	15.6	24.2	687.9	0.6	4.12	-	2.9	22.2	15.6	0.50	S		F82 (5)
S78	6861	353.18	-0.01	-82.5±1.5	8.8±0.4	5	42.8	20.3	28.5	666.4	0.5	3.86	-	1.1	3.6	19.4	-	S		
S79	7275	357.14	-0.09	-7.4±1.8	2.7±2.0	5	17.0	7.7	2.5	145.7	0.5	5.57	-	5.6	14.6	0.9	0.17	S	Scu-Cen	GMF358 (1)
S80	7443	357.71	-0.34	4.7±1.6	21.3±4.4	12	327.3	141.6	1318.4	4028.2	0.7	4.71	-	13.0	-148.1	4.1	0.55	C	Scu-Cen	Fil8 (2)
S81	7686	359.69	-0.00	-72.1±40.5	8.4±4.6	17	157.3	82.5	1295.3	8236.8	3.7	8.23	-	0.1	6.1	3.1	0.07	L,H		
S82	7701	359.66	-0.10	-30.4±12.2	8.2±0.1	11	102.7	39.1	592.8	5770.5	2.9	4.02	-	0.1	-7.5	8.5	0.07	S,H		
S83	7736	0.10	-0.07	42.3±23.3	8.4±5.4	64	137.1	51.6	3634.2	26504.2	6.1	3.69	-	0.1	-3.0	2.1	0.14	C		
S84	8513	6.44	-0.44	20.0±3.4	3.6±1.0	14	24.0	11.1	13.2	550.5	0.9	4.60	-	4.8	-10.2	19.8	0.09	S,H	Scu-Cen	
S85	8591	5.53	-0.32	13.2±1.3	2.9±1.4	9	30.1	13.0	4.5	150.9	0.4	5.29	-	5.5	3.1	18.3	0.57	S	Scu-Cen, Bone	
S86	8624	5.82	-0.48	17.3±1.3	3.4±1.2	7	22.5	9.1	16.5	736.4	1.1	4.44	-	5.0	-11.2	0.8	0.02	S	Scu-Cen	
S87	9021	8.27	-0.43	17.2±1.9	2.7±1.0	5	29.0	11.3	5.1	174.6	0.3	3.63	-	5.7	-1.0	28.2	-	S	Scu-Cen, Bone	
S88	9707	12.84	0.03	32.7±0.6	3.4±0.6	5	19.4	9.6	3.8	193.5	0.6	3.67	-	5.1	19.7	5.0	-	C	Scu-Cen	
min		0.10	-0.69	-193.2	2.0	5	13.0	6.9	0.3	17.3	0.0	2.04	1.65	0.1	-148.1	0.1	0.01			
max		359.69	0.44	170.0	21.3	64	327.3	141.6	3634.2	26504.2	6.1	20.82	6.10	13.0	98.0	87.9	0.57			
med		327.54	-0.07	-33.9	8.4	7	56.6	33.3	14.4	242.6	0.4	4.27	2.70	5.4	3.3	23.7	0.13			
mean		228.64	-0.05	-21.3	8.6	8	65.5	35.8	98.5	846.7	0.6	5.09	2.94	5.0	-2.6	32.8	0.17			
Std		155.09	0.26	62.9	4.6	7	48.7	24.3	432.0	3000.9	0.8	2.38	1.12	2.4	47.1	27.0	0.16			
S		-0.71	0.00	0.7	0.4	6	2.4	1.2	6.9	7.5	4.7	3.72	0.99	0.1	-0.8	0.7	1.10			
K		-1.47	-0.91	1.5	-0.5	42	8.6	2.4	50.6	59.7	26.1	20.21	0.02	1.9	0.6	-0.9	0.35			

Notes. Columns are:
(1) ID: Assigned filament ID
(2) Origin: The identification algorithm for M1-M55 is MST, and the SEDIGISM cloud IDs (Duarte-Cabral et al. 2021) for leaves contained in each filament are listed in Table. C.1. For S56-S88, the identification algorithm is SCIMES, and the original SEDIGISM cloud IDs (Duarte-Cabral et al. 2021), one per filament, are listed here.
(3) l_{wt} (deg): Flux-weighted Galactic longitude for M1-M55, and Galactic longitude of the cloud's centroid for S56-S88
(4) b_{wt} (deg): Flux-weighted Galactic latitude for M1-M55, and Galactic latitude of the cloud's centroid for S56-S88
(5) v_{wt} (km s^{-1}): Flux weighted velocity for M1-M55, and system velocity for S56-S88
(6) d (kpc): Distance, the median of all leaf distances for M1-M55, and final adopted distance for S56-S88
(7) N: The number of leaves in the filament
(8) $L_{\rm sum}$ (pc): The sum of "edge" lengths (separation of each two connected leaves) for M1-M55 and medaxis length for S56-S88
(9) L_{end} (pc): End-to-end length along the major axis for M1-M55, and major axis for S56-S88. To define the major axis of a filament, we plot all the leaves belonging to this filament in the projected sky (Galactic longitude as x and Galactic latitude as y) and fit a line with principle component analysis Pearson (PCA 1901) as the major axis of this filament
(10) Mass ($10^3\,M_\odot$): Mass of the filament, derived by summing leaf mass for M1-M55, and cloud mass for S56-S88
(11) M_{line} ($M_\odot$ pc^{-1}): Line mass, mass per unit length (Mass/$L_{\rm sum}$)
(12) N_{H_2} (10^{22} cm^{-2}): H_2 column density
(13) f_A: Aspect ratio
(14) f_L: Linearity, the ratio between the spread (standard deviation) of leaves along the major axis and spread along the minor axis, only for M1-M55
(15) R_{gc} (kpc): Galactocentric radius, the median of leaf Galactocentric radius for M1-M55, and cloud Galactocentric radius for S56-S88
(16) z (pc): Height above Galactic mid-plane
(17) $|\theta|$ (deg): Orientation angle between filaments major axes and Galactic mid-plane in the projected sky
(18) DGMF: Dense gas mass fraction, the ratio between dense gas mass and total mass of the filaments
(19) Mor.: Morphology class following Wang et al. (2015), "L" represents linear straight L-shape, "C" bent C-shape, "S" quasi-sinusoidal shape, "X" crossing of multiple filaments, "H" head-tail or hub-filament system
(20) Arm: The nearest arm the filaments associated. If a filament is also a bone, "Bone" is added after the arm name. For inter-arm filaments, the value is empty. We propose eight bones, they are M6, M24, S66, S67, S71, S72, S85, and S87.
(21) Ref: References to previously known filaments. (1) means Abreu-Vicente et al. (2016), (2) for Zucker et al. (2015), (3) for Jackson et al. (2010), (4) for Wang et al. (2016), (5) for Ge & Wang (2022)
Some of the properties are derived differently for filaments identified through leaves with MST (with the ID of M1-M55) and filaments selected from SEDIGISM clouds (with the ID of S56-S88), such as $L_{\rm sum}$, L_{end}, f_A, and $|\theta|$. Most of the physical properties for S56-S88 are adopted from Duarte-Cabral et al. (2021). The last seven rows show the statistics of the filament properties. Skewness measures the asymmetry of a probability distribution. For instance, the normal distribution has $S = 0$. Negative skewness means that the tail is on the left side of the distribution, and on the right side for the positive skewness. Kurtosis characterizes how the distribution is shaped compared to a normal distribution. The normal distribution has $K = 0$. A distribution with $K > 0$ is more centrally peaked than normal distribution while for $K < 0$ is flatter.

Appendix B: Influence of different spiral arm models

To investigate to what degree different spiral arm models will affect our results, we tested two other spiral arm models. One is the model in Reid et al. (2019, R19 model, hereafter). It fits log-periodic spirals to the locations of masers and extend to the fourth Galactic quadrant with arm tangencies. Another recent spiral arm model was constructed by Hou (2021, H21 model, hereafter). This one summarizes good spiral tracers such as giant molecular clouds, high-mass star-formation region masers, HII regions, O-type stars, and young open clusters to depict the nearby spiral arms. These two spiral arm models are overlaid on the Taylor & Cordes (1993) model (TC93 model, hereafter) in Fig. B.1. On the whole, the three spiral arm models are consistent with each other. However, some differences remain, as described in the following. In the PV space, the three models have the most significant difference for the Normal-Outer arm. In the face-on view, nearby arms in the R19 model and the H21 model show consistency. At the beginning of the Norma-Outer arm, the TC93 model has a large separation from the R19 model and the H21 model. In the fourth Galactic quadrant, the Norma-Outer arm, Scutum-Centaurus arm, and Sagittarius-Carina arms exhibit visbible differences with respect to the R19 and TC93 models. The number of filaments associated with each arm in PV space differs with respect to different models, but the number of bones is six for the R19 model, similarly to the TC93 model (eight bones). The difference in mean DGMFs for on-arm filaments and off-arm filaments is a factor of 1.1 if we use the H21 model and 1.4 for the R19 model. Differences in mean DGMFs for different arms are less than 10% if we use the R19 model. For the H21 model, the mean DGMF in the Scutum-Centaurus Arm is about twice that of the Norma Arm. The statistics on different spiral models are summarized in Table B.1.

Table B.1: Summary of basic statistics based on different spiral models.

Model	On-arm filaments	Off-arm filaments	Number of bones	DGMFs for on-arm	DGMFs for off-arm
TC93	44	44	8	0.173	0.171
R19	25	63	6	0.200	0.146
H21	14	74	3	0.155	0.178

Notes. The first column lists the spiral models used. TC93 for Taylor & Cordes (1993), R19 for Reid et al. (2019), and H21 for Hou (2021). The second column lists the number of filaments associated with spiral arms for each spiral model and the third column lists the number of filaments that are not associated with any arms. The fourth column lists the number of filaments satisfying the criteria for bones. The fifth column lists mean DGMF for filaments associated with spiral arms, while the sixth column lists those "of"f arms.

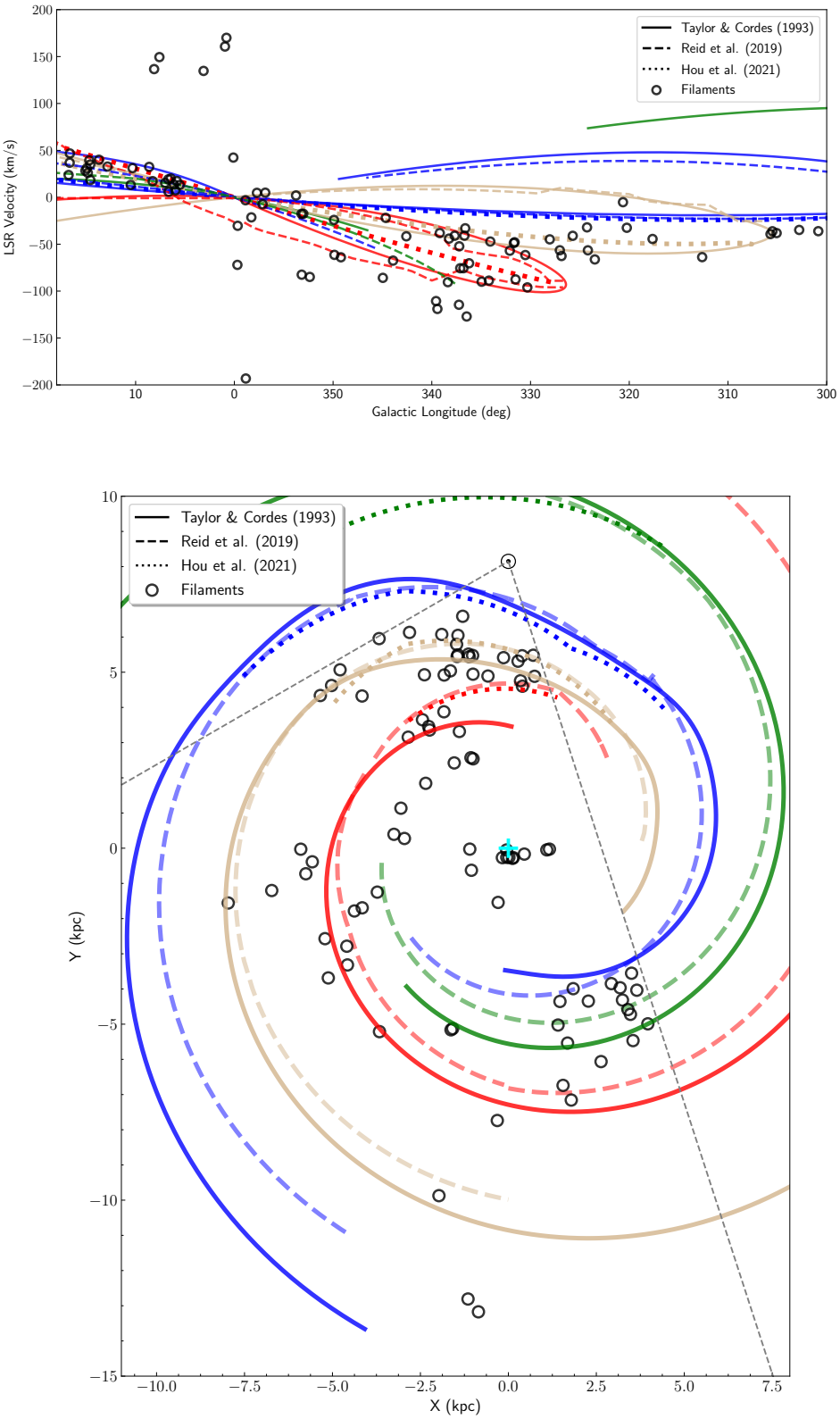

Fig. B.1: Different spiral arm models. The top panel is a longitude–velocity view of filaments and spiral arms. Spiral arms from Taylor & Cordes (1993), Reid et al. (2019), and Hou (2021) are plotted as solid lines, dashed lines, and dotted lines, respectively. Red, brown, blue, and green represent the Norma-Outer, Scutum-Centaurus, Sagittarius-Carina, and Perseus arms, respectively. Black circles denote our filaments. The bottom panel is a face-on view of filaments and spiral arms. The cyan plus symbol represents the Galactic center, and the grey dashed lines show the data range.

Appendix C: Original SEDIGISM cloud IDs of leaves in MST filaments

For filaments identified through leaves with MST (with IDs of M1-M55), the original SEDIGISM cloud ids of the leaves contained in each filament are listed in Table. C.1.

Table C.1: Original SEDIGISM cloud IDs of leaves in MST filaments

Filament ID	SEDIGISM cloud id
M1	[40, 44, 47, 48, 54, 55]
M2	[101, 110, 115, 155, 156, 158]
M3	[248, 254, 255, 257, 259, 264, 333]
M4	[272, 317, 348, 349, 350, 351]
M5	[1697, 1699, 1701, 1702, 1791, 1798]
M6	[1984, 1986, 1987, 1988, 2098, 2099, 2100, 2101, 2102, 2103]
M7	[2014, 2017, 2019, 2020, 2125, 2126, 2127]
M8	[2199, 2222, 2363, 2367, 2368, 2372]
M9	[2235, 2239, 2393, 2397, 2400, 2401, 2403, 2615, 2637]
M10	[3524, 3542, 3543, 3546, 3547, 3804, 3806, 3808, 3809, 3824]
M11	[3691, 3693, 3699, 3702, 3708, 4006, 4009]
M12	[3907, 3908, 3912, 3913, 3914, 4186, 4198]
M13	[4224, 4226, 4230, 4239, 4241, 4543, 4544, 4551, 4560, 4562]
M14	[4346, 4348, 4623, 4628, 4629, 4632]
M15	[4420, 4422, 4423, 4424, 4673, 4684]
M16	[4160, 4161, 4162, 4466, 4467, 4469]
M17	[4714, 4904, 4913, 4915, 4918, 4924]
M18	[4597, 4598, 4600, 4842, 4850, 4852, 4853]
M19	[4063, 4067, 4366, 4372, 4374, 4376]
M20	[4793, 4803, 4805, 4815, 5070, 5072]
M21	[5523, 5524, 5531, 5533, 5679, 5680, 5684]
M22	[5618, 5623, 5743, 5750, 5826, 5841]
M23	[2122, 2123, 2276, 2281, 2282, 2285]
M24	[6215, 6220, 6224, 6322, 6324, 6328, 6337, 6339, 6346]
M25	[6546, 6547, 6554, 6697, 6698, 6699, 6700, 6704]
M26	[6614, 6615, 6618, 6621, 6762, 6767, 6768, 6769, 6770, 6771, 6774, 6777]
M27	[6761, 6766, 6948, 6951, 6952, 6953, 6962, 6970, 6975]
M28	[6868, 6873, 6897, 6939, 6942, 6961]
M29	[7205, 7211, 7215, 7216, 7310, 7315, 7317, 7320]
M30	[7399, 7538, 7541, 7542, 7543, 7544]
M31	[7434, 7435, 7441, 7564, 7567, 7578, 7586]
M32	[7369, 7484, 7488, 7490, 7491, 7492]
M33	[7896, 7897, 7898, 7899, 7901, 8033, 8036]
M34	[7891, 8022, 8024, 8026, 8027, 8028]
M35	[8252, 8254, 8256, 8257, 8258, 8260]
M36	[8484, 8493, 8528, 8595, 8606, 8612, 8616, 8617, 8681, 8682, 8735, 8742, 8760, 8765]
M37	[8413, 8414, 8416, 8430, 8432, 8533, 8558, 8559, 8563, 8579, 8583]
M38	[8514, 8538, 8564, 8580, 8633, 8767, 8768]
M39	[8499, 8523, 8544, 8652, 8659, 8667, 8669]
M40	[8626, 8707, 8723, 8724, 8876, 8879]
M41	[8816, 8817, 8818, 8971, 8972, 8973]
M42	[8963, 8964, 8965, 9023, 9036, 9077, 9081]
M43	[8918, 9067, 9068, 9071, 9073, 9074, 9082]
M44	[9190, 9198, 9203, 9206, 9214, 9362]
M45	[9250, 9253, 9266, 9269, 9270, 9272, 9423]
M46	[9735, 9746, 9972, 9974, 9981, 9983, 9992, 9993, 9995, 9998, 10018, 10020, 10024]
M47	[9913, 9917, 9921, 9923, 9928, 10132, 10152]
M48	[9930, 9931, 10140, 10154, 10161, 10163, 10164]
M49	[9875, 9882, 9887, 9888, 10102, 10105, 10107, 10108, 10115, 10116, 10118]
M50	[9940, 9941, 9947, 9950, 9951, 9952, 9953, 9957, 10172]
M51	[9978, 9979, 10180, 10185, 10191, 10196, 10207, 10208]
M52	[10131, 10139, 10143, 10147, 10150, 10388, 10392]
M53	[10299, 10312, 10336, 10338, 10556, 10568, 10579, 10580]
M54	[10403, 10404, 10531, 10540, 10550, 10553]
M55	[10472, 10482, 10484, 10485, 10487, 10491, 10497, 10503]

Notes. The first column lists IDs of our filaments identified by means of the MST approach. The second column shows the origin SEDIGISM cloud ids (Duarte-Cabral et al. 2021) of the leaves that the filament includes.

Appendix D: Comparison of the results from the MST and the SCIMES

As we combine the filaments identified by the MST algorithm and filaments selected from clouds identified by the SCIMES algorithm to obtain a filament sample, the differences between the two methods should be examined. We split the 33 SCIMES filaments in our catalog (S56-S88) into leaves and apply the MST to the leaves. We find that 11/33 can be recovered by the MST without any changes in parameters. For example, S75 is shown in the top panel of Fig.D.1. We can see, the MST successfully connects the leaves of S75. If we only slightly change the parameters for the MST, another 17 SCIMES filaments can be re-connected. An example is S56 shown in the middle panel of Fig.D.1. To re-connect the leaves, the matching velocity is changed from 2 km s^{-1} to 3.4 km s^{-1}. For the other five SCIMES filaments, the parameters should change much to re-connect them (e.g., S59, bottom panel of Fig.D.1). One leaf (the bottom pink circle) is too far from the others (the top four pink ones) to be connected. As a result, the number of leaves cannot reach five, and it is thus eliminated by the MST algorithm. Thus, the two methods have similarities as most of the filaments identified by the SCIMES can be reconnected by the MST. However, they are also focused differently and are complementary, which offers a more complete sample.

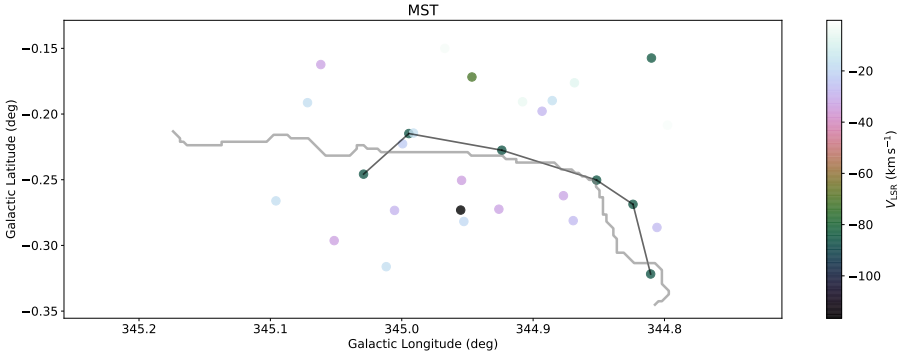

(a)

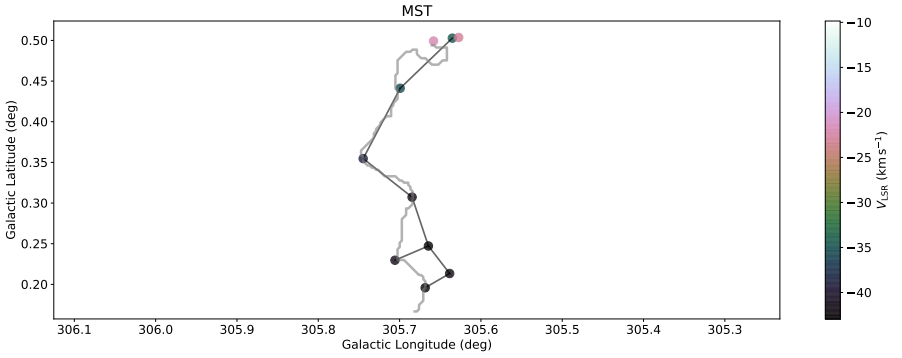

(b)

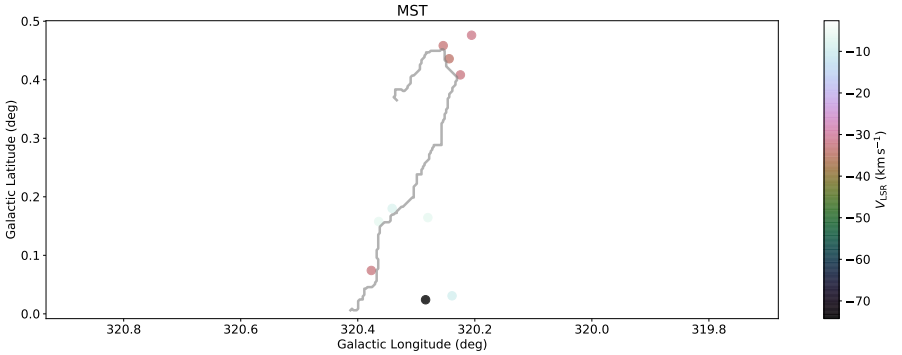

(c)

Fig. D.1: Re-connecting SCIMES filaments with MST. Circles are SEDIGISM leaves color coded with velocity. The color bars show their radial velocities. Black line segments are MST edges and gray curves are SCIMES filament spines.

Appendix E: Two color views of filaments

We have displayed several filaments in Fig. 1. Two color composite images of all the filaments are shown in Fig. E.1. The color-coded circles denote leaves in filaments with different velocities. For M1-M55, white line segments are edges. For S56-S88, white curves are their medial axis. For backgrounds, cyan represents intermediate infrared 24 μm emission on a logarithmic scale from MIPSGAL (Carey et al. 2009), and red shows integrated ^{13}CO(2-1) emission in linear scale.

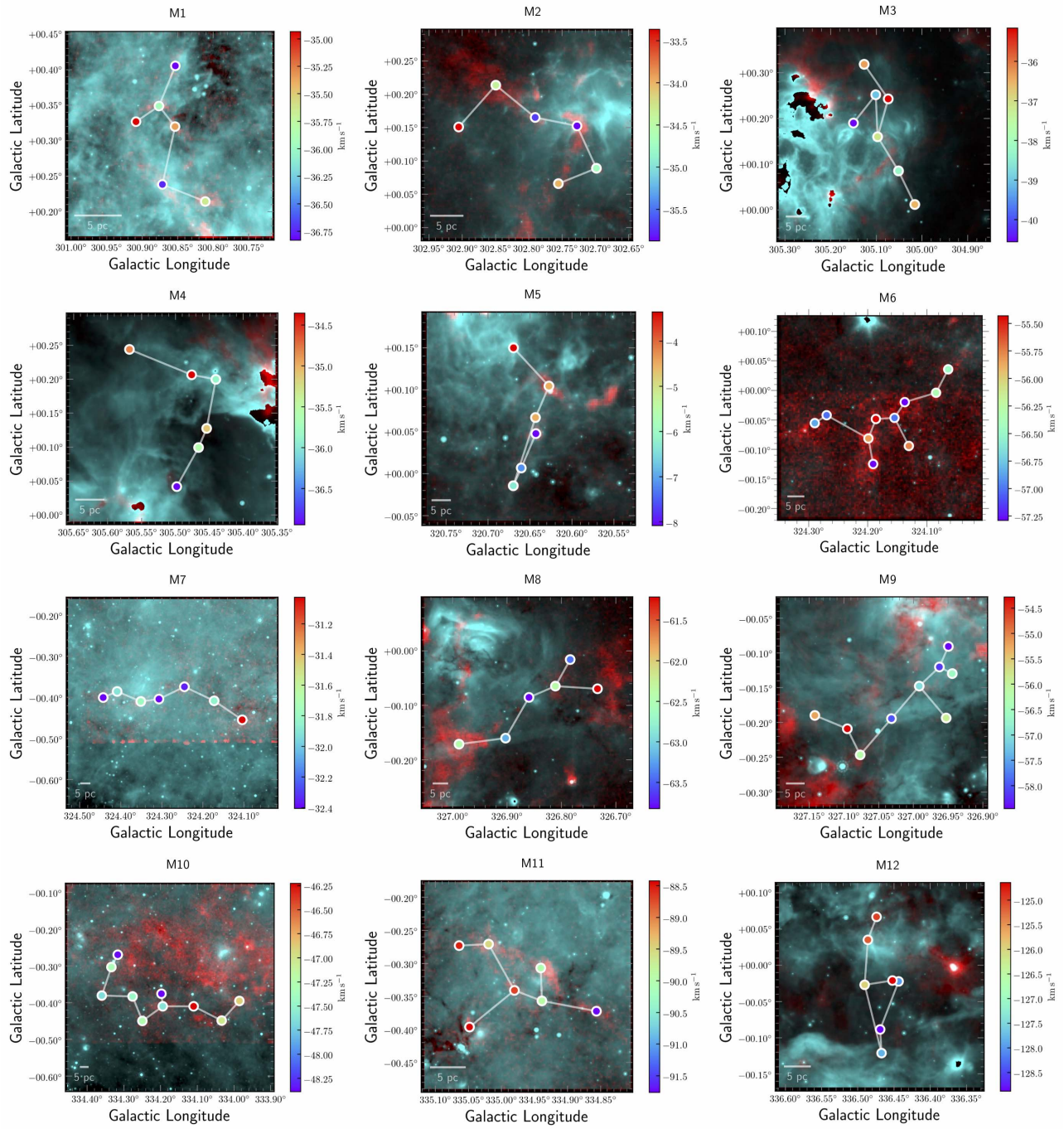

Fig. E.1: Two-color view of filaments. The color-coded circles denote leaves in filaments with different velocities. For M1-M55, the white line segments are edges. For S56-S88, the white curves are their medial axis. For backgrounds, cyan represents intermediate infrared 24 μm emission on a logarithmic scale from MIPSGAL (Carey et al. 2009) and red shows s integrated ^{13}CO(2-1) emission.

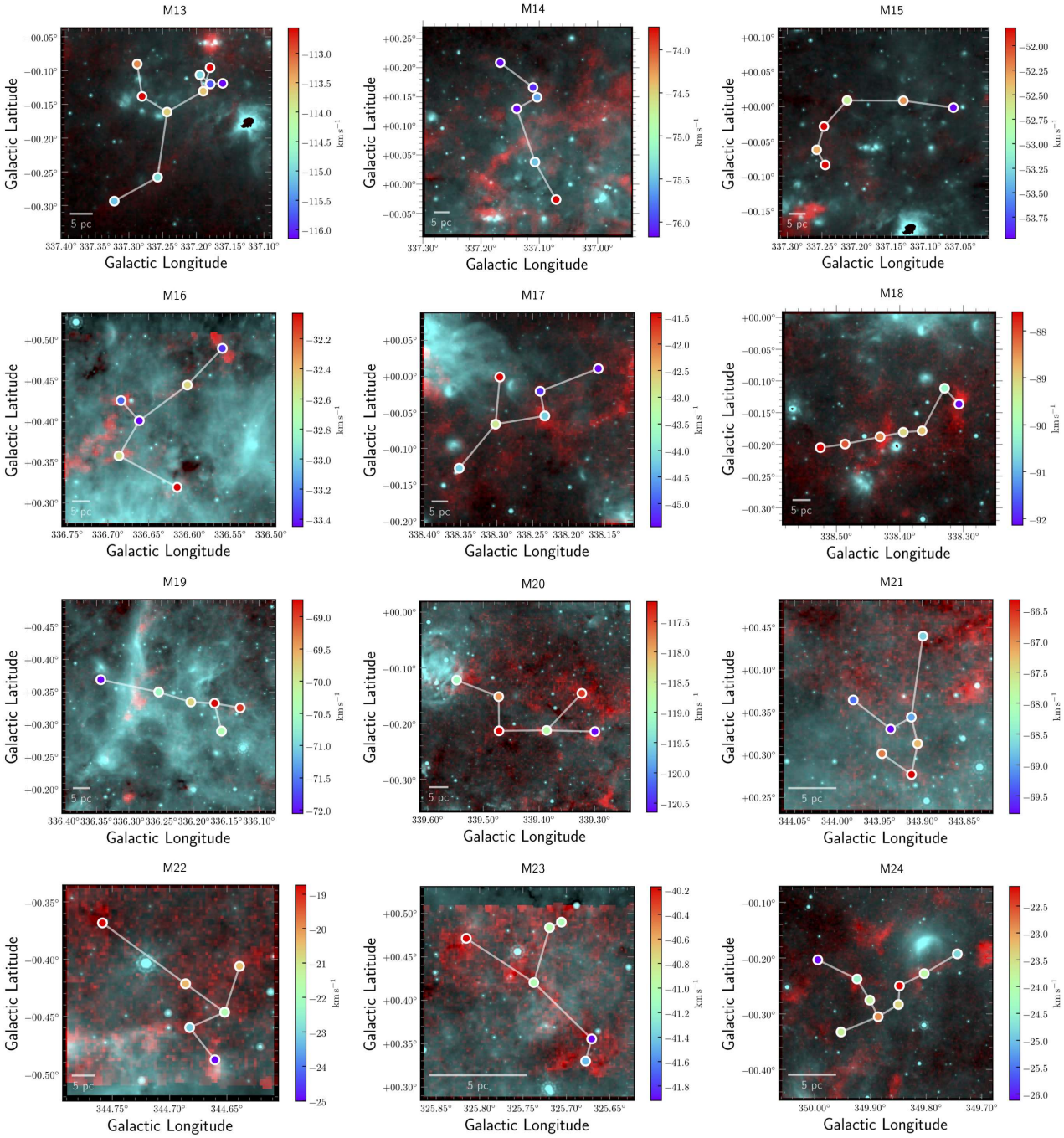

Fig. E.1: continued: M13-M24

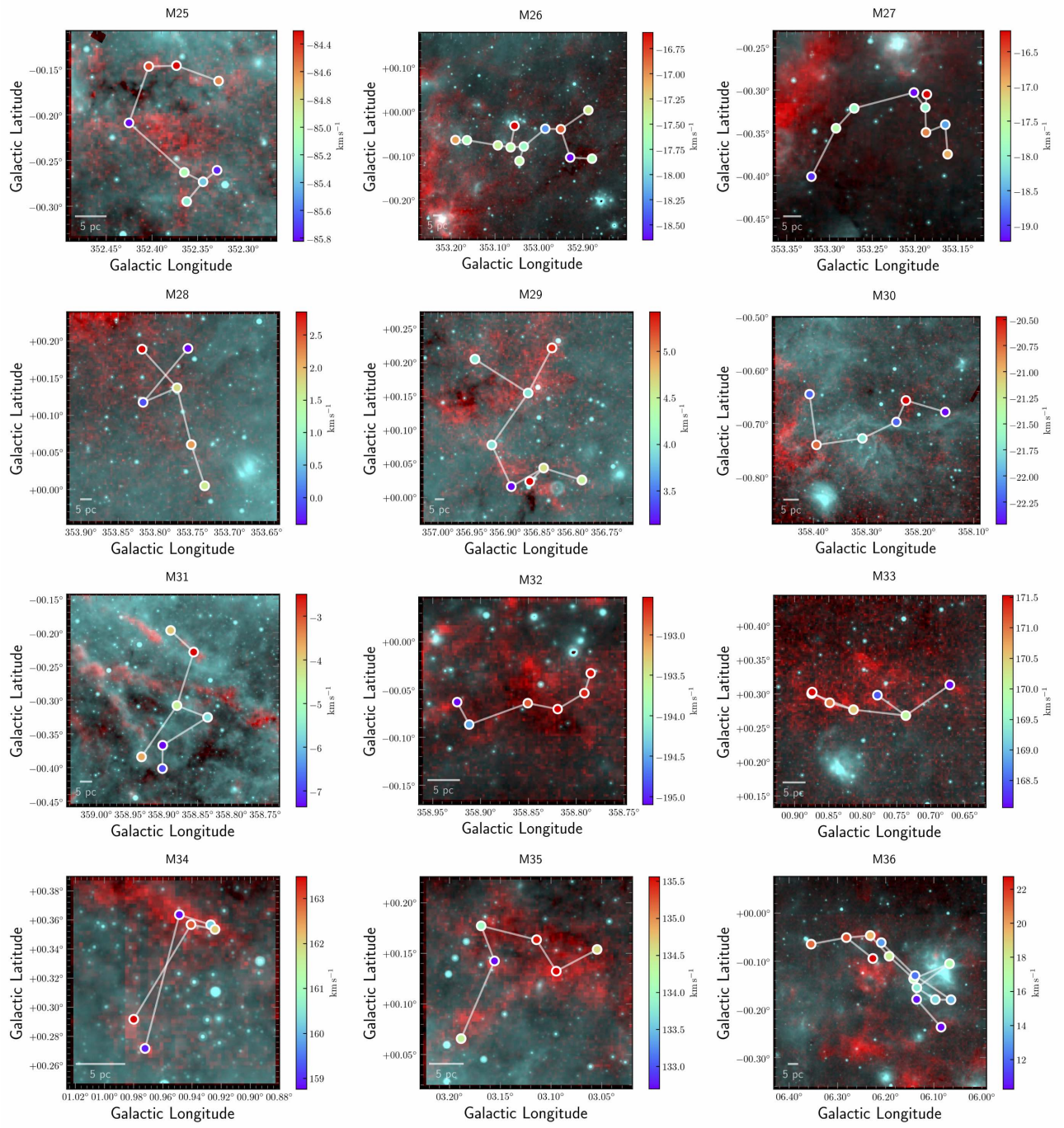

Fig. E.1: continued: M25-M36

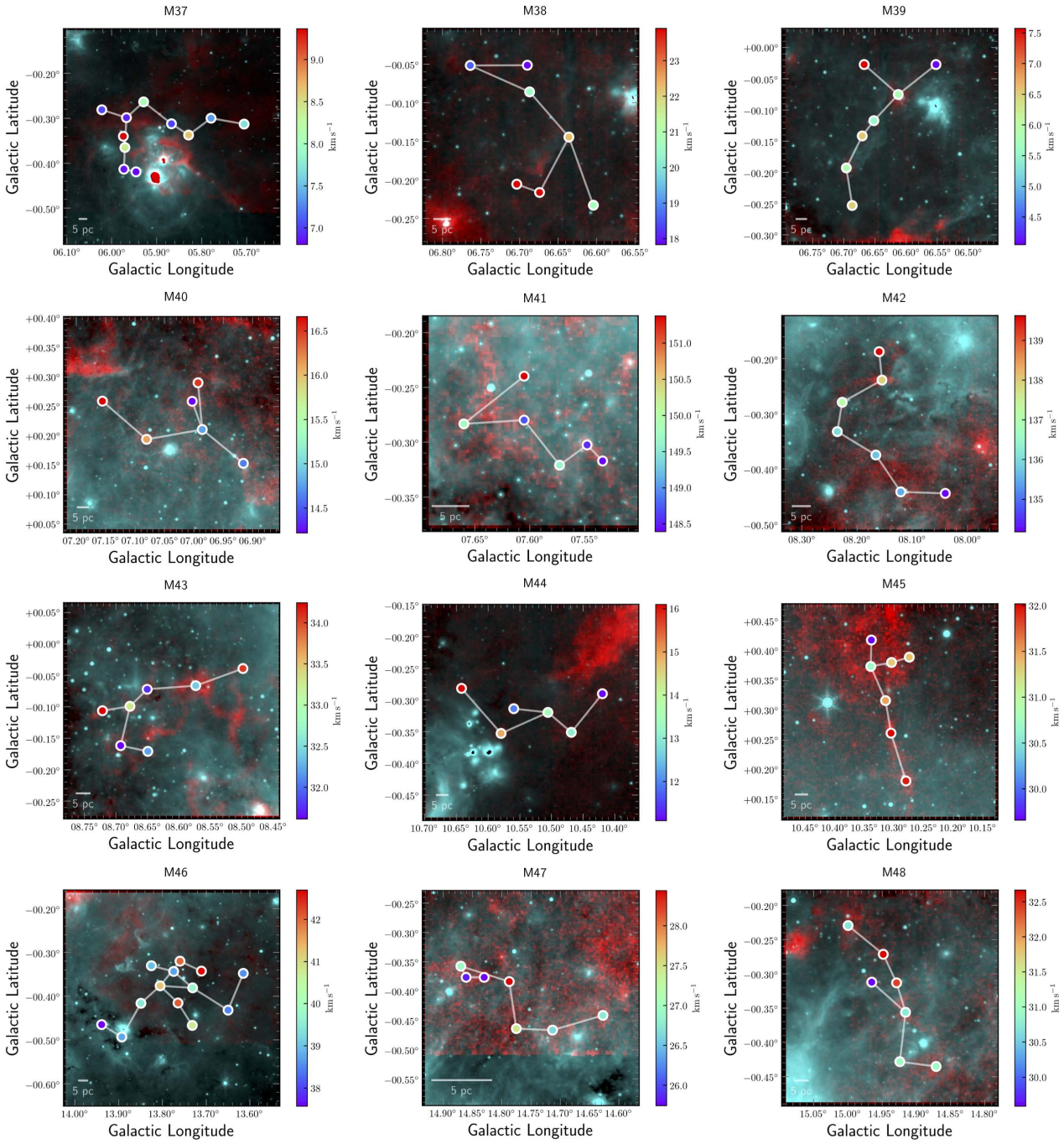

Fig. E.1: continued: M37-M48

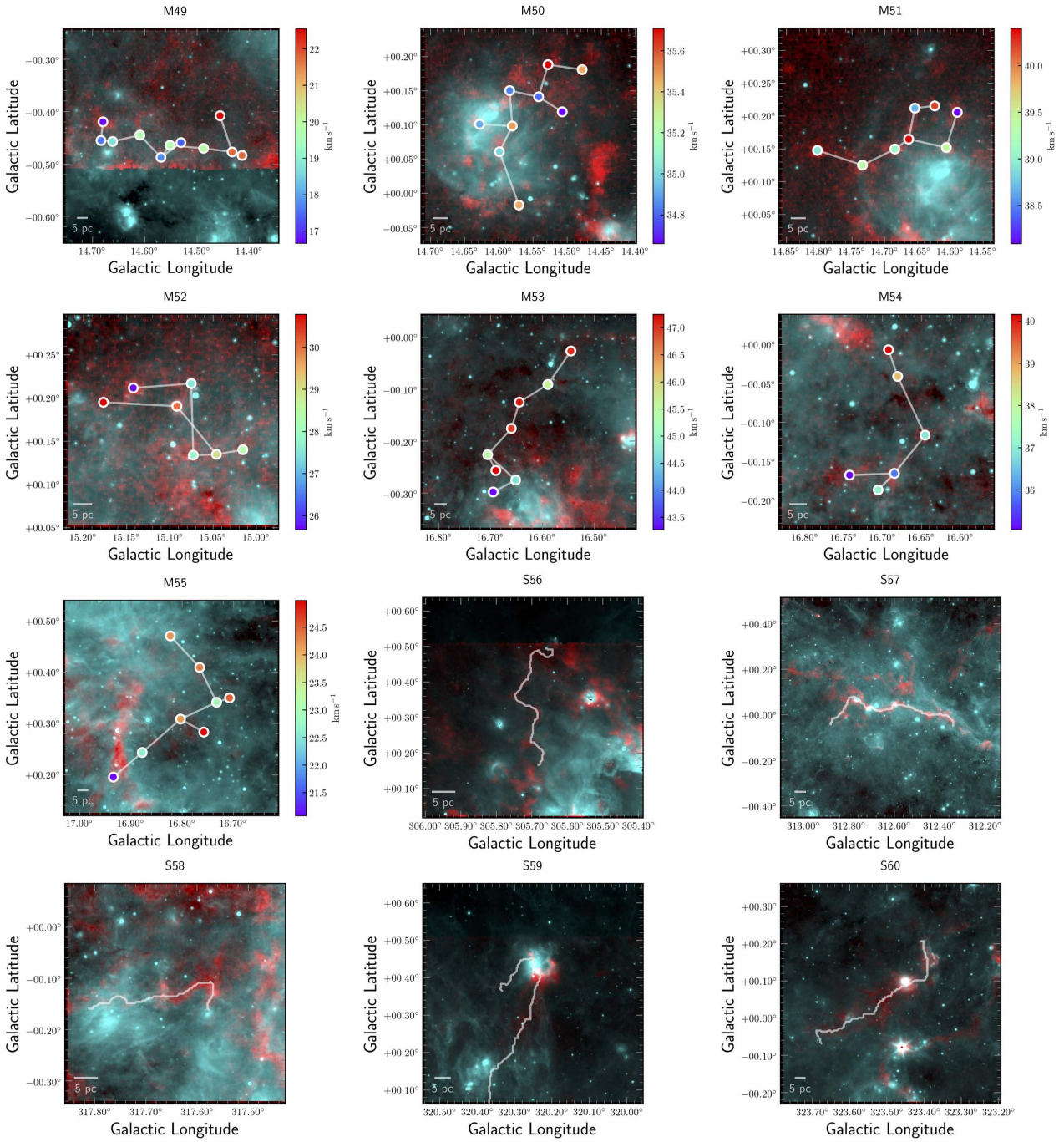

Fig. E.1: continued: M49-M55 & S56-S60

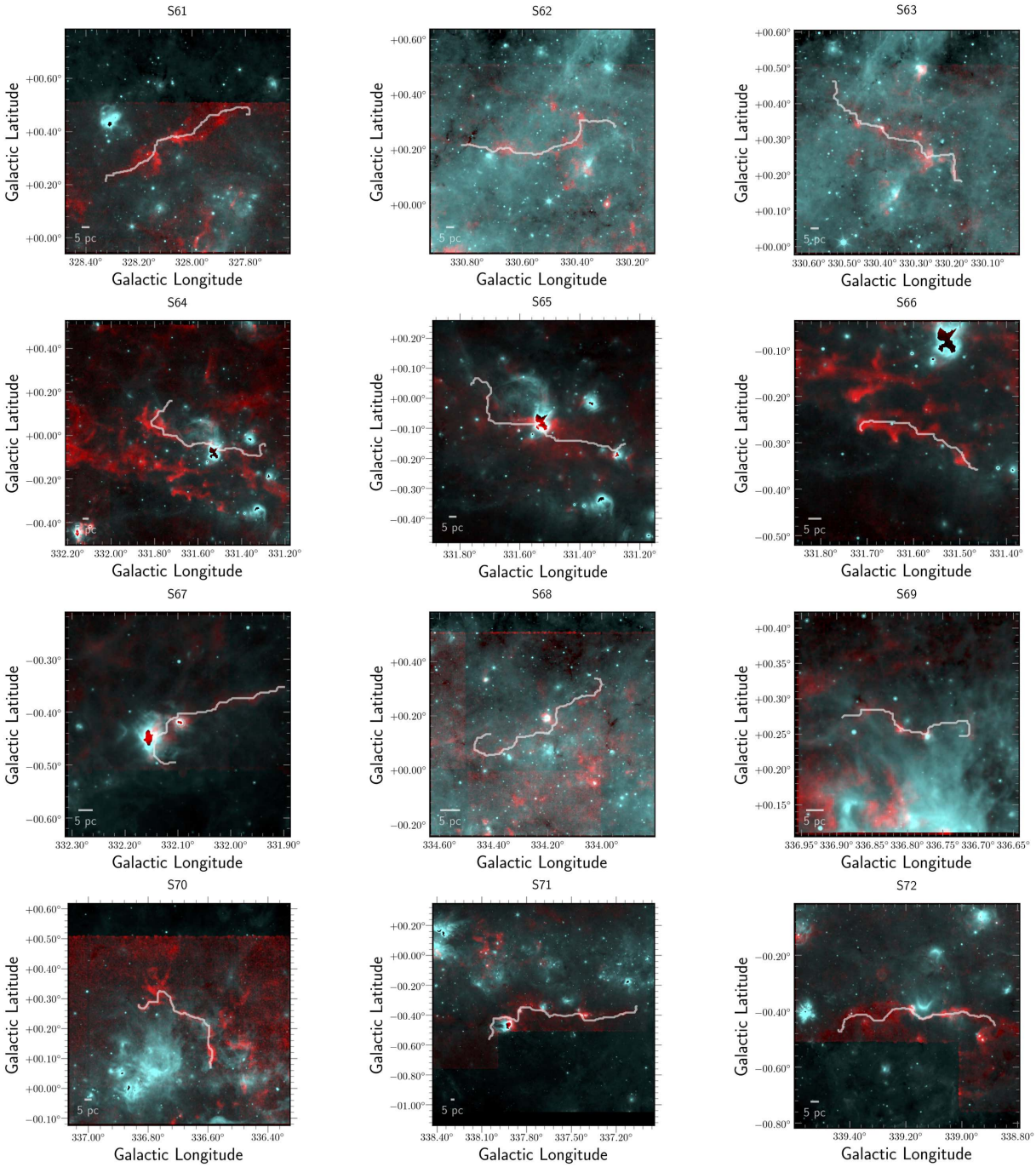

Fig. E.1: continued: S61-S72

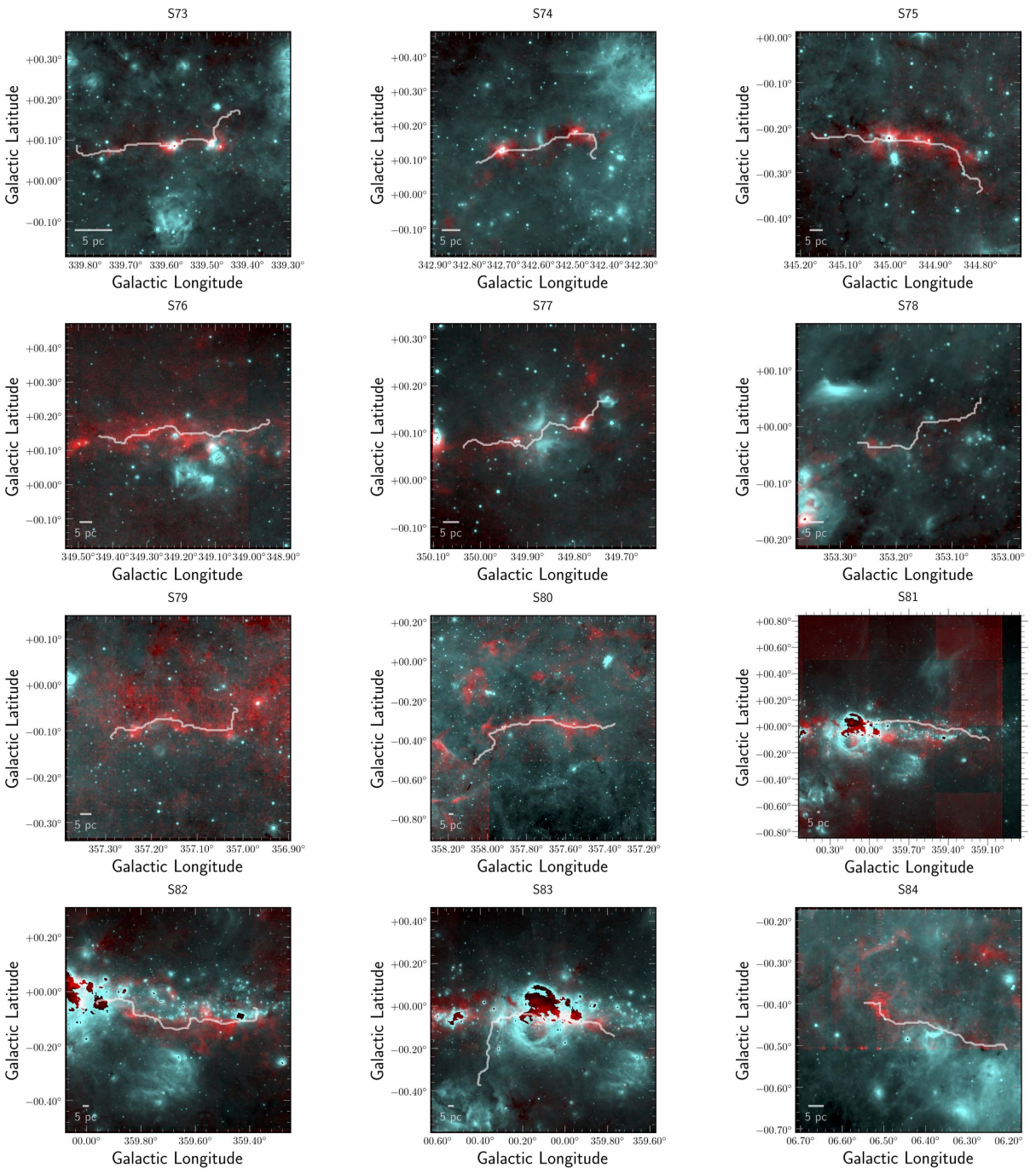

Fig. E.1: continued: S73-S84

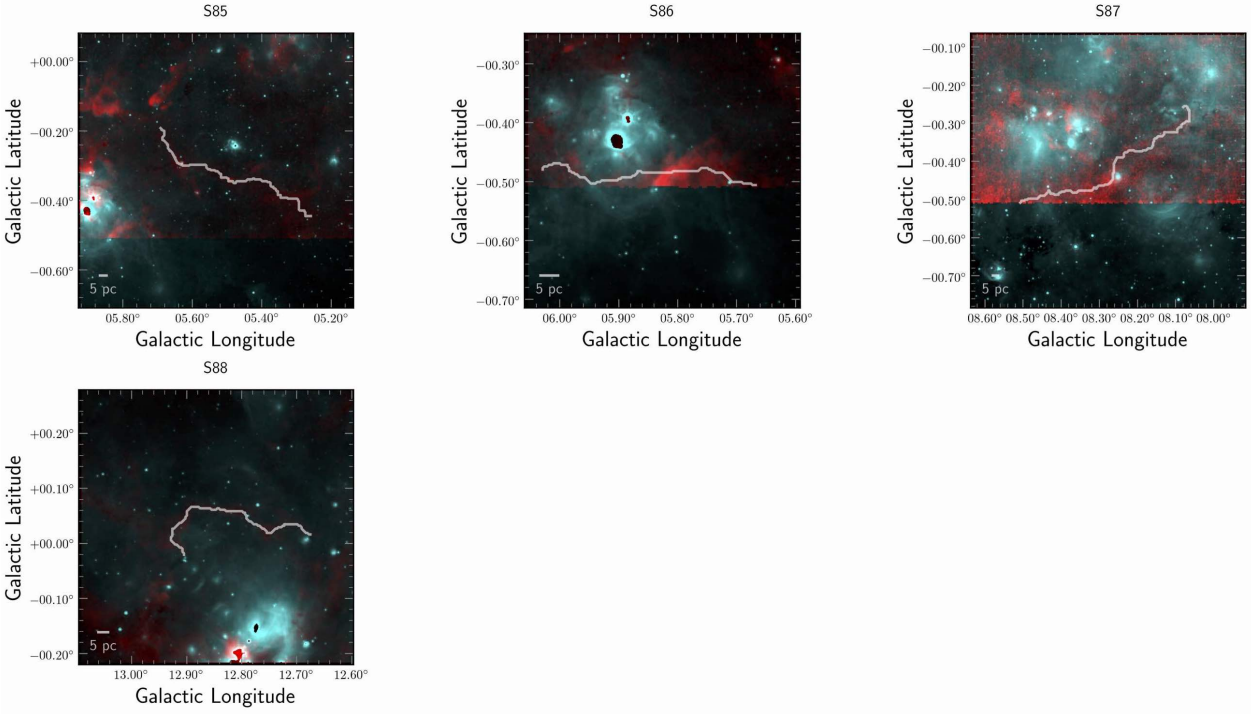

Fig. E.1: continued: S85-S88